THE ASTROPHYSICAL JOURNAL, 476:781–800, 1997 February 20

DISCOVERY OF A HIGHLY COLLIMATED MOLECULAR OUTFLOW IN THE SOUTHERN BOK GLOBULE BHR 71

TYLER L. BOURKE,[1,2] GUIDO GARAY,[3] KIMMO K. LEHTINEN,[4] IVE KÖHNENKAMP,[3] RALF LAUNHARDT,[5] LARS-Å. NYMAN,[6] JORGE MAY,[3] GARRY ROBINSON,[1] AND A. R. HYLAND[1,7]
Received 1996 April 4; accepted 1996 September 11

ABSTRACT

We report observations of the southern Bok globule BHR 71 in the $J = 1 \rightarrow 0$ and $J = 2 \rightarrow 1$ lines of ^{12}CO, the $J = 1 \rightarrow 0$ lines of ^{13}CO and $C^{18}O$, and $(J, K) = (1, 1)$ and (2, 2) inversion lines of NH_3 made with angular resolution of $\sim 20''$ to $\sim 9'$. We also report 1.3 mm continuum observations made with SEST with $\sim 20''$ resolution. The low angular resolution molecular observations indicate that the globule has a diameter of ~ 0.5 pc, a kinetic temperature of 11 K, a total mass of $\sim 40\ M_\odot$, and an average molecular density of $\sim 9 \times 10^3$ cm^{-3}. The high angular resolution observations reveal the presence, near the center of the globule, of a highly collimated bipolar outflow with lobes extending by ~ 0.3 pc in opposite directions from a strong 1.3 mm continuum source. The morphology and velocity structure of the flow is found to be well described by a biconical outflow that is inclined from the line of sight at an angle of $\sim 84°$, has a semi-opening angle of 15°, and in which the gas moves outward with an approximate constant radial velocity (with respect to the cone apex) of ~ 28 km s^{-1}. The outflow appears to be driven by a very young stellar object with $L_{bol} \sim 9\ L_\odot$, whose characteristics at infrared and millimeter wavelengths are similar to those of the so-called Class 0 sources.

Subject headings: ISM: globules — ISM: individual (BHR 71) — ISM: jets and outflows — ISM: structure

1. INTRODUCTION

Bok & Reilly (1947) first suggested that small (angular sizes of a few arcminutes) dark clouds, now known as Bok globules, might be gravitationally unstable and hence potential sites for the formation of low-mass stars. This hypothesis has proven to be correct by a wealth of infrared and submillimeter observations, which show that the presence of heavily obscured low-mass embedded sources in Bok globules is quite common (e.g., Yun & Clemens 1990, 1994, 1995; Launhardt & Henning 1994). Further, there is increasing observational evidence that as they are being formed, low-mass stars undergo periods of copious mass loss. This ubiquitous phenomenon is observationally manifested by the presence of Herbig-Haro objects (see review by Reipurth 1991), optical jets (see review by Mundt 1988), and highly supersonic molecular outflows (see reviews of Bachiller & Gómez-González 1992; Fukui et al. 1993; Bachiller 1996; and references therein). In most cases the spatial structure of the ejected gas is bipolar. The nature of this phenomenon is, however, still poorly understood.

In recent years a new class of outflows have been identified: the highly collimated outflows of which L1448 (Bachiller et al. 1990; Bachiller, Martín-Pintado, & Planesas 1991) is the prototype. The discovery of these highly collimated outflows has had a strong influence on the theoretical study of bipolar outflows and has resulted in a series of new models in which the driving source is a highly collimated, mostly atomic jet (e.g., Masson & Chernin 1993; Raga & Cabrit 1993). There is general agreement that the highly collimated outflows represent the earliest stage in outflow evolution and that understanding their nature will provide new insights into the mechanism at work driving all bipolar outflows.

An equally important discovery is that of a new class of young stellar objects (YSOs), which may very well be the true low-mass protostars, i.e., the bulk of their final stellar matter has not yet been assembled. Dubbed "Class 0" sources (André, Ward-Thompson, & Barsony 1993, hereafter AWB) in the spirit of the Lada (1991) classification scheme, these sources are characterized as having a strong submillimeter luminosity compared to their bolometric luminosity, having a narrow spectral energy distribution (SED) that is well represented by a blackbody of temperature 15–30 K, showing no emission at wavelengths below 10 μm, and having indirect evidence for a central YSO, for example a highly collimated outflow (Barsony 1994; André 1995). In addition, submillimeter observations show that they possess large amounts of circumstellar dust, typically a factor 10 greater than Class I sources (e.g., Bontemps et al. 1996). Simple arguments indicate that these sources have ages of a few $\times 10^4$ yr, and all the various evolutionary diagrams that have been proposed for YSOs point to the Class 0 sources as being very young (e.g., AWB; Myers & Ladd 1993; Bontemps et al. 1996). However, the expected number of Class 0 YSOs at any given time is expected to be low, due to the short lifetime of this evolutionary stage (Barsony 1994), and this has been borne out observationally (e.g., AWB). Thus, identifying and studying new Class 0 sources is important for the development of star formation theories.

[1] School of Physics, University College, The University of New South Wales, Australian Defence Force Academy, Canberra, ACT 2600, Australia.
[2] SAO Predoctoral Fellow. Present address: Harvard-Smithsonian Center for Astrophysics, 60 Garden Street, MS 42, Cambridge, MA 02138; tbourke@cfa.harvard.edu.
[3] Departamento de Astronomía, Universidad de Chile, Casilla 36-D, Santiago, Chile.
[4] Helsinki University Observatory, Tähtitorninmäki, P.O. Box 14, SF-00014, University of Helsinki, Finland; kklehtinen@cc.helsinki.fi.
[5] Max Planck Society Research Unit "Dust in Star-Forming Regions," Schillergäßchen 2-3, D-07745 Jena, Germany.
[6] European Southern Observatory, Casilla 19001, Santiago 19, Chile.
[7] Present address: Office of the Vice Chancellor, Southern Cross University, Lismore, NSW 2480, Australia.

Due to their simple geometry and environment, isolated globules are among the best suited objects for a detailed study of the process of formation of individual stars. The dark cloud BHR 71 (Bourke, Hyland, & Robinson 1995a; a.k.a. Sa136 [Sandqvist 1977], DC 297.7−2.8 [Hartley et al. 1986]) is an excellent example of an isolated opaque Bok globule. It is located near the southern Coalsack and has an angular size at optical wavelengths of 8′ × 3′ (Hartley et al. 1986). It appears in the H_2CO survey of southern dark clouds by Goss et al. (1980), the ^{12}CO survey of the Carina Arm by Grabelsky et al. (1987) and the NH_3 survey of southern hemisphere globules by Bourke et al. (1995b). Bourke et al. (1995b) mapped the dense ammonia core in BHR 71, and from their observations derived a core mass of $\sim 3\ M_\odot$ (corrected from Bourke et al. for the new distance estimate of 200 pc—see Seidensticker & Schmidt-Kaler 1989) and a kinetic temperature of 13 K. Maps of the *IRAS* emission toward this object, made using the co-added images from the *IRAS* Sky Survey Atlas, show the presence of two infrared sources projected toward the globule. One of them, IRAS 11590−6452, is projected near the center of the globule and is heavily obscured, suggesting that a low-mass star has been formed, or is in the process of formation, in the innermost region of BHR 71.

Near-infrared observations of BHR 71 by Bourke et al. (1993; see also Bourke 1994) shows that bipolar-like nebulosity is visible either side of IRAS 11590−6452, suggesting that a molecular outflow may be present in BHR 71. In this paper we present observations of BHR 71 in lines of ^{12}CO, ^{13}CO, $C^{18}O$, and NH_3, and continuum observations at 1.3 mm, with angular resolutions ranging from 20″ to 9′. We report the discovery of a highly collimated bipolar molecular outflow in BHR 71, centered on IRAS 11590−6452. We also report the detection of a strong 1.3 mm continuum source, which is coincident with IRAS 11590−6452. We find that this source corresponds to a cold object ($T_{\rm dust} \sim 35$ K), with a core-envelope structure and a total luminosity of $L_{\rm bol} \sim 9\ L_\odot$. The observed and derived characteristics suggest that the driving source of the outflow is a very young stellar object, possibly a new example of a Class 0 protostar.

2. OBSERVATIONS

The observations were made using the 1.2 m Millimeter Wave Radio Telescope at the Cerro Tololo Inter-American Observatory (CTIO), Chile, the 15 m Swedish–ESO Submillimetre Telescope (SEST) located on La Silla, Chile, and the Parkes 64 m radio telescope in Australia. The basic observing parameters are summarized in Table 1.

2.1. *CTIO Radio Telescope*

The observations with the CTIO radio telescope of the emission in the ^{12}CO $J = 1 \rightarrow 0$ ($\nu = 115271.201$ MHz) and ^{13}CO $J = 1 \rightarrow 0$ ($\nu = 110201.370$ MHz) lines from BHR 71 were undertaken during 1994 May–June and 1995 May, respectively. At the observed frequencies the half-power beam width of the telescope was $\sim 8\farcm8$. The receiver was a liquid nitrogen–cooled Schottky receiver (see Bronfman et al. 1988 for a description). The spectrometer consisted of a 256 channel filter bank, each channel being 100 kHz wide. This provided velocity resolutions of 0.26 and 0.27 km s^{-1} at the frequencies of the ^{12}CO $J = 1 \rightarrow 0$ and ^{13}CO $J = 1 \rightarrow 0$ lines, respectively.

In the ^{12}CO $J = 1 \rightarrow 0$ line we mapped, with an angular spacing of 3′.75, a region $\sim 40'$ in diameter. In each of the 100 positions observed we integrated until the rms noise per channel was reduced to 0.20 K in main-beam temperature (antenna temperature corrected for main-beam efficiency; $\eta_{\rm mb} = 0.82$). Typically, this was achieved after integrating for about 12 minutes per position. In the ^{13}CO $J = 1 \rightarrow 0$ line we mapped, with an angular spacing of 3′.75, a region $\sim 30'$ in diameter. In each of the 50 positions observed we integrated for 20 minutes, reaching typically an rms noise per channel in main-beam temperature of 0.13 K.

2.2. *Swedish–ESO Submillimetre Telescope*

2.2.1. ^{12}CO *and* ^{13}CO *Observations*

The observations of ^{12}CO $J = 1 \rightarrow 0$ and ^{13}CO $J = 1 \rightarrow 0$ line emission using SEST were undertaken during 1994 April and 1995 April, September, and October. In the 3 mm range the telescope was equipped with dual-polarization Schottky mixer receivers (1994 April and 1995 April) or SIS receivers (1995 September–October). The telescope beam size at the observed frequencies was $\sim 45''$ (FWHM) and the main beam efficiency was 0.70. Most of the observations were performed in frequency-switched mode. Higher signal-to-noise observations were performed in position-switched mode, with the OFF position located at $\alpha_{1950} = 11^{\rm h}53^{\rm m}44\fs7$ and $\delta_{1950} = -65°13'58''$.

In the ^{12}CO $J = 1 \rightarrow 0$ transition we observed 177 positions within a $\sim 200'' \times 480''$ region with 20″ spacing in frequency-switched mode. The system temperatures varied between 350 and 900 K, depending on weather conditions and observing session (in 1995 September and October the new SIS receiver was used, which resulted in significantly lower system temperatures), and the resulting rms noise in antenna temperature was between 0.2 and 0.9 K for an integration time of 50 s. In position-switched mode a region of 6′ × 10′ in size was mapped with 60″ spacing (50 positions). The system temperatures were in the range 530–590 K. The integration time on source at each position was 2 minutes, resulting in an rms noise of typically 0.2 K in antenna temperature. In all the ^{12}CO observations the back end used was a high-resolution acousto-optical spectrometer with 1000 channels and a velocity coverage of ~ 112 km s^{-1} for frequency-switched observations, and 2000 channels with a velocity coverage of ~ 225 km s^{-1} for position-switched observations. The resolution in both cases was 0.112 km s^{-1}.

In the ^{13}CO $J = 1 \rightarrow 0$ transition we observed 34 positions with 60″ spacing in position-switched mode, and 50 positions with 90″ spacing over a 9′ × 9′ region in frequency-switched mode. The 1000 channels provided a velocity resolution of 0.118 km s^{-1} and a velocity coverage of ~ 117 km s^{-1}. The system temperatures were ~ 220 K for the position-switched observations and ~ 350 K for the frequency-switched observations. The integration time on source at each position was 3 minutes (position-switched) or 1 minute (frequency-switched), resulting in a rms noise in a single spectral line channel of typically 0.08 or 0.25 K in antenna temperature, respectively.

Observations of ^{12}CO $J = 2 \rightarrow 1$ ($\nu = 230538.000$ MHz) were undertaken in 1994 April and 1995 April with 20″ spacing about the center of the globule and at the CO peaks in the outflow lobes, simultaneously with the $J = 1 \rightarrow 0$ observations. System temperatures varied between 600–750

TABLE 1

SUMMARY OF OBSERVATIONAL PARAMETERS

Observation	Frequency (GHz)	Beam (FWHM)	Spacing	Positions Observed	Δv (km s^{-1})	rms Noise (K)
CTIO Radio Telescope						
^{12}CO $J = 1 \rightarrow 0$	115.271	8.8	3.75	100	0.26	0.20
^{13}CO $J = 1 \rightarrow 0$	110.201	8.8	3.75	50	0.27	0.13
SEST Radio Telescope						
^{12}CO $J = 1 \rightarrow 0$	115.271	45″	60″	50	0.112	0.20
			20″	177		0.50
^{13}CO $J = 1 \rightarrow 0$	110.201	47″	60″	34	0.117	0.08
			90″	50		0.25
C^{18}O $J = 1 \rightarrow 0$	109.782	47″	40″	93	0.118	0.10
^{12}CO $J = 2 \rightarrow 1$	230.538	23″	20″	36	0.056	0.50
1.3 mm continuum	236 ($\Delta v = 50$)	23″	...	7 maps	...	...
Parkes Radio Telescope						
NH_3 (J, K) = (1, 1).....	23.694	84″	60″	30	0.12/0.05	0.03
NH_3 (J, K) = (2, 2).....	23.722	84″	60″	5	0.12/0.05	0.03

K. Observations were frequency-switched, and the 1000 channels of the spectrometer provided a velocity coverage of 56 km s^{-1} with a velocity resolution of 0.056 km s^{-1}. Integration times were the same as for the $J = 1 \rightarrow 0$ observations, 50 s, resulting in an rms noise of $\sim$0.5 K. The effective beam size at 1 mm is $\sim$23″ (FWHM), and the main beam efficiency is 0.60.

2.2.2. C^{18}O *Observations*

Observations of C^{18}O $J = 1 \rightarrow 0$ ($\nu = 109782.160$ MHz) were undertaken in 1994 April. We observed 93 positions in frequency-switched mode within a 6.7 × 6.7 region with 40″ spacing. The 1000 channels of the spectrometer provided a velocity coverage of $\sim$118 km s^{-1} with a velocity resolution of 0.118 km s^{-1}. System temperatures were $\sim$330 K, and the on-source integration time was 2 minutes per position, resulting in an rms noise in antenna temperature of $\sim$0.1 K.

2.2.3. *Continuum Observations*

The continuum observations were carried out during 1995 November using the SEST single channel bolometer operating at 1.3 mm. The bolometer has a center frequency of 236 GHz and a bandwidth of $\sim$50 GHz. It consists of a Germanium element inside a ^{3}He cryostat cooled to about 0.3 K. A similar bolometer is described by Kreysa (1990). At 1.3 mm the telescope has an effective beamwidth of 23″ (FWHM). Beam switching was done with a focal plane chopper having a horizontal beam throw of 70″. Seven maps were obtained by scanning in azimuth at a rate of 8″ s^{-1}, with adjacent scans separated by 8″ in elevation (about one-third of the beamwidth). Pointing was done on a nearby quasar and found to be repeatable to within $\pm$3″. The atmospheric transmission was measured by skydips every 2 hours. Focus measurements were done more frequently after sunrise and sunset. The zenith opacities varied during the observing run (two nights) and were in the range $0.13 < \tau < 0.28$. Uranus was used as the calibrator source and was assumed to have a brightness temperature of 96 K at 236 GHz. The flux calibration is believed to be accurate to 20%, the uncertainty being caused mainly by the limited accuracy of the adopted calibrator temperature. The raw data were corrected for atmospheric attenuation and transformed into NOD2 format (Haslam 1974) using SEST software. Final data reduction was done with the software package MAP (written by R. Zylka, MPIfR Bonn) that uses the NOD2 and GAG libraries. The double-beam maps were restored into single-beam maps using an improved algorithm of Emerson, Klein, & Haslam (1979), shifted, averaged (weighted by their rms noise, resulting in a final map with an rms noise level of $\sim$35 mJy beam^{-1}), and transformed from an azimuth-elevation system into the equatorial coordinate system.

2.3. *Parkes Radio Telescope*

Ammonia observations of BHR 71 have previously been reported by Bourke et al. (1995b), and full details of the observational techniques can be found there. Observations of BHR 71 were undertaken at the Parkes radio telescope in the (J, K) = (1, 1) and (2, 2) transitions of NH_3 at 23.694495 and 23.722633 GHz, respectively, during 1991 November and 1994 February. In 1991 November the old Parkes 1024-channel digital correlator was split into two sections of 512 channels, providing a velocity resolution of 0.12 km s^{-1}. The globule was mapped in the (1, 1) line at 30 positions with 60″ spacing about the Hartley et al. (1986) position ($\alpha_{1950} = 11^h59^m10^s$, $\delta_{1950} = -64°52'24''$), and both transitions were also observed at the *IRAS* PSC position ($\alpha_{1950} = 11^h59^m03^s.1$, $\delta_{1950} = -64°52'11''$). In 1994 February the new Parkes 16384-channel digital correlator was split into two sections of 2048 channels, providing a resolution of 0.05 km s^{-1}. Mapping was performed in the (1, 1) line with 30″ spacing centered on the *IRAS* position in a 13 point cross, and five positions were simultaneously observed in the (2, 2) transition. Absolute calibration of the 1994 observations are uncertain, so the (1, 1) mapping results from this session are not used. However, since the (1, 1) and (2, 2) observations were undertaken simultaneously absolute calibration is not important for the derivations of properties using these transitions. The beamwidth at these frequencies was $\sim$84″.

3. RESULTS

3.1. *Globule Characteristics*

Optical images of BHR 71, in blue and far-red light, are shown in Figure 1. The image on the left is from the UK

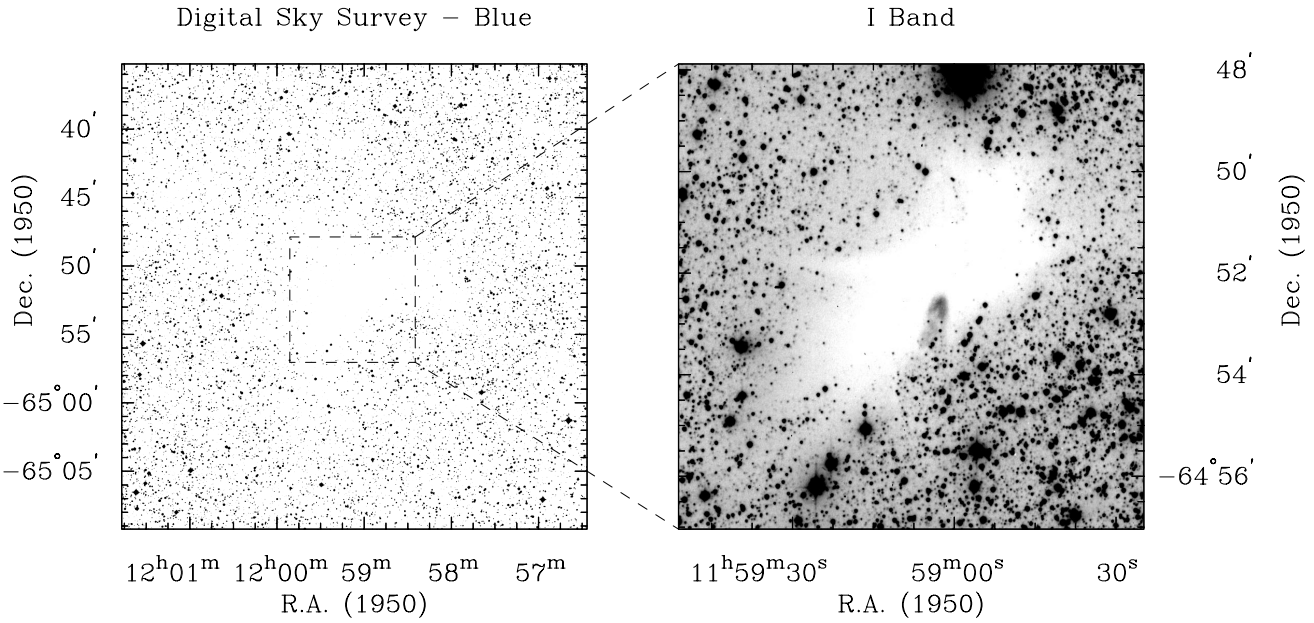

FIG. 1.—Optical images of the Bok globule BHR 71. *Left*: the UK Schmidt IIIaJ image, taken from the Digital Sky Survey (DSS). The FOV is ∼35′ on a side. The lack of stars toward the center clearly defines the globule. *Right*: *I*-band image taken with a 1024 × 1024 pixel TEK CCD on the 1 m telescope at Siding Spring Observatory. The FOV is ∼9′ on a side. The opacity of the globule is evident in this image, as well as a conical shaped nebulosity protruding from near its center.

Schmidt IIIaJ survey plate and was obtained from the Digital Sky Survey (DSS),[8] while the image on the right is an *I*-band image taken in 1993 January with a 1024 × 1024 pixel TEK CCD on the 1 m telescope of the Mount Stromlo and Siding Spring Observatories, located at Siding Spring, Australia. The coordinate system of both images was determined by comparison with stars from the *Hubble Space Telescope* Guide Star Catalog (1989). In the DSS image, the Bok globule nature of the cloud is clearly evident—it is well isolated and very opaque. In the *I*-band image, the central region of the globule is still very opaque, despite the large number of background stars present. Nebulosity is also visible in the *I*-band image, hinting at its active star-forming state. In fact, stars may be seen through the nebulosity, suggesting that a hole or cavity has been created there. From its association (positional and velocity) with the Coalsack, Bourke et al. (1995b) estimated the distance to BHR 71 at 175 pc, based on the work of Rodgers (1960). However, more recent determinations of the distance to the Coalsack (Seidensticker & Schmidt-Kaler 1989) place it nearer to 200 pc. We adopt a value of 200 pc as the distance to BHR 71. Conversion between angular and linear size is thus 1′ ∼ 0.06 pc, or 1.′7 ∼ 0.1 pc.

3.1.1. ^{12}CO *and* ^{13}CO

Maps of the velocity integrated ^{12}CO and ^{13}CO emission from BHR 71 overlayed on the DSS image are shown in Figure 2. The range of velocity integration is from −6 to −3 km s^{-1} for both molecules. The ^{12}CO $J = 1 \rightarrow 0$ emission arises from roughly a circular region, with observed major and minor axis of 14.′5 and 14.′2 (full width at half-power), respectively. The deconvolved sizes, computed by assuming that the observed size is the quadrature sum of the true cloud size and the telescope beam (8.′8), both assumed to have Gaussian shapes, are 11.′5 and 11.′1 (0.68 × 0.65 pc). The emission in the ^{13}CO $J = 1 \rightarrow 0$ line is elongated in a direction with position angle (PA) of ∼125°, having observed major and minor axes of 14.′2 and 11.′2, respectively. The deconvolved major and minor axes for ^{13}CO are 11.′1 and 6.′9, respectively (0.65 × 0.40 pc). Unlike the well studied Bok globule B335, the molecular emission is well centered on the region of greatest visual extinction (Frerking, Langer, & Wilson 1987). The slight extension to the northeast traces a low visual extinction region seen more clearly on the original Schmidt plate. From the profiles of the ^{12}CO $J = 1 \rightarrow 0$ and ^{13}CO $J = 1 \rightarrow 0$ emission integrated over the source, we determined line center velocities of −4.26 and −4.35 km s^{-1}, and line widths of 1.09 ± 0.01 and 0.80 ± 0.02 km s^{-1}, respectively.

3.1.2. $C^{18}O$ *and* NH_3

In Figure 3 we show integrated $C^{18}O$ and NH_3 maps overlayed on the *I*-band image. The range of velocity integration is the same as for Figure 2. Both maps show a relatively elongated core with position angles of ∼126° and ∼117°, respectively. The deconvolved map sizes (FWHM) are 5.′3 × 2.′5 for $C^{18}O$ and 3.′5 × 2.′1 for NH_3, which imply linear sizes of 0.31 × 0.15 pc and 0.20 × 0.12 pc, respectively. As discussed by Myers (1995), a molecular cloud does not have a unique size, its dimension and appearance in a particular map being a strong function of the tracer used to observe it. The ammonia observations most likely trace the denser gas within the globule core, while $C^{18}O$ is tracing the column density. The $C^{18}O$ contours match very well the extinction in the *I*-band image but indicate some nonuniformities in column density, which are discussed in § 5.1. The ammonia contours show a relatively symmetric dense

[8] The Digitized Sky Survey was produced at the Space Telescope Science Institute under US Government grant NAG W-2166. The UK Schmidt Telescope was operated by the Royal Observatory Edinburgh with funding from the UK Science and Engineering Research Council (later the UK Particle Physics and Astronomy Research Council), until 1988 June, and thereafter by the Anglo-Australian Observatory. The blue plates of the southern Sky Atlas and its Equatorial Extension (together known as the SERC-J), as well as the Equatorial Red (ER), and the Second Epoch (red) Survey (SES), were all taken with the UK Schmidt.

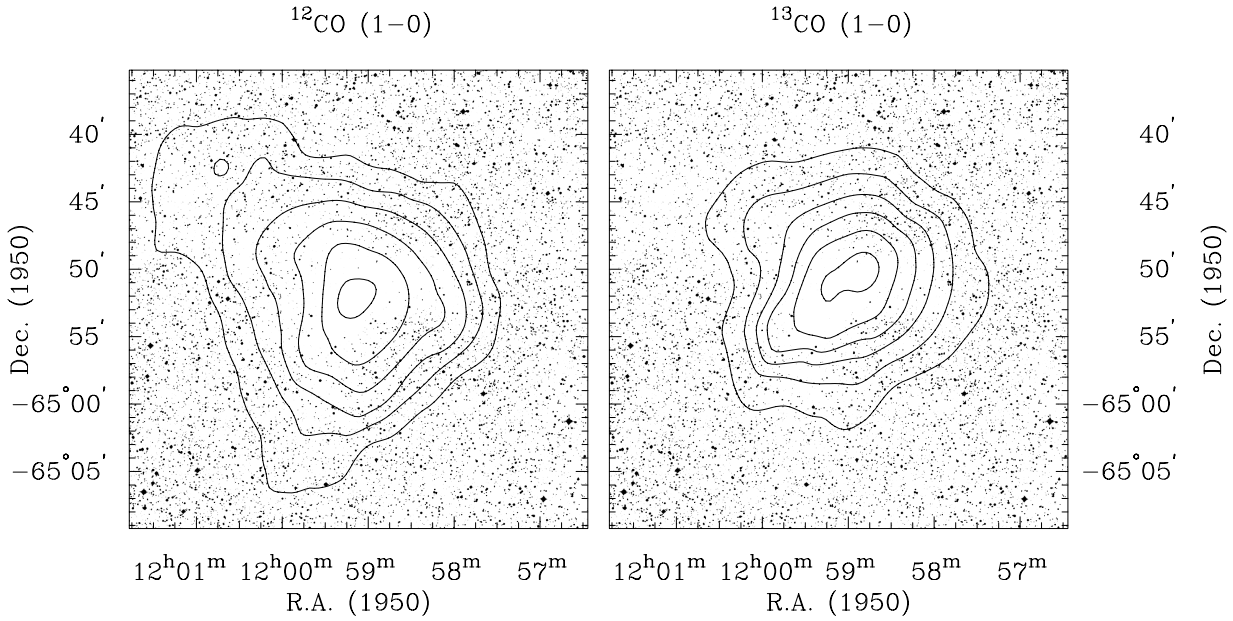

FIG. 2.—Integrated CO maps of BHR 71 (CTIO). *Left*: ^{12}CO $J = 1 \rightarrow 0$ emission integrated over the velocity range $-6 < v_{lsr} < -3$ km s^{-1}, overlayed on the *I*-band image. The contour levels are 20%, 35%, 50%, 65%, 80%, and 95% of the peak $\int T_{mb}\, dv$ of 10.0 K km s^{-1}. *Right*: ^{13}CO $J = 1 \rightarrow 0$ emission integrated over the same velocity range as the ^{12}CO emission. The contour levels are 20%, 35%, 50%, 65%, 80%, and 95% of the peak $\int T_{mb}\, dv$ of 2.8 K km s^{-1}.

core, with a slight elongation to the northwest. However, the beam size used (84″) does not allow a detailed study of the density structure. From the sum of all C^{18}O spectra across the source we determine $V_{lsr} = -4.63$ km s^{-1} and ΔV (FWHM) $= 0.82 \pm 0.01$ km s^{-1}. For NH_3 we determine $V_{lsr} = -4.45$ km s^{-1} and $\Delta V = 0.69 \pm 0.03$ km s^{-1} (using the higher spectral resolution observations and fitting the ammonia hyperfine structure). We will assume a cloud velocity of ~ -4.5 km s^{-1} for future discussion.

3.2. *Molecular Outflow*

3.2.1. *Morphology*

Figure 4 shows the ^{12}CO $J = 1 \rightarrow 0$ spectra across a $6' \times 10'$ region of BHR 71, mapped with SEST in position-switched mode. Strikingly seen in this figure is the presence toward the northwest of strong emission at velocities redshifted with respect to the systemic dark cloud velocity of ~ -4.5 km s^{-1}, and toward the southeast the presence of

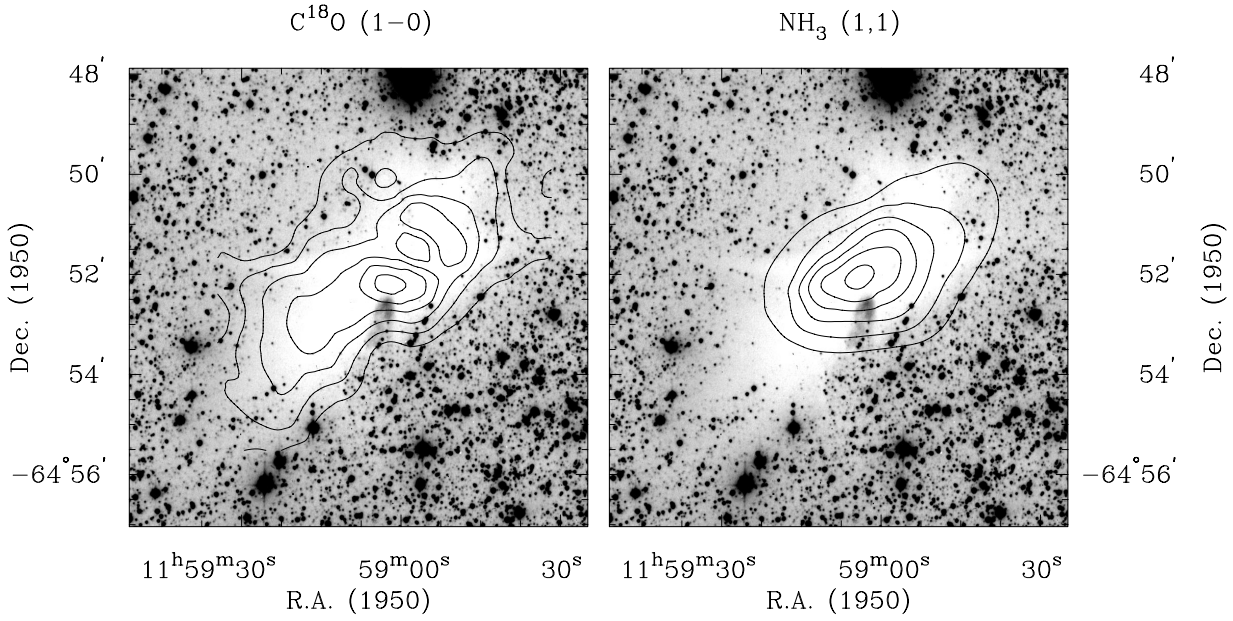

FIG. 3.—Integrated emission in the lines of C^{18}O $J = 1 \rightarrow 0$ (SEST) and NH_3 $(J, K) = (1, 1)$ (Parkes). *Left*: C^{18}O map, integrated over the velocity range $-6 < v_{lsr} < -3$ km s^{-1}, overlayed on the *I*-band image. The contour levels are 20%, 35%, 50%, 65%, 80%, and 95% of the peak $\int T_{mb}\, dv$ of 2.4 K km s^{-1}. *Right*: NH_3 $(J, K) = (1, 1)$ emission integrated over the same velocity range as the C^{18}O emission. The contour levels are 20%, 35%, 50%, 65%, 80%, and 95% of the peak $\int T_{mb}\, dv$ of 3.8 K km s^{-1}.

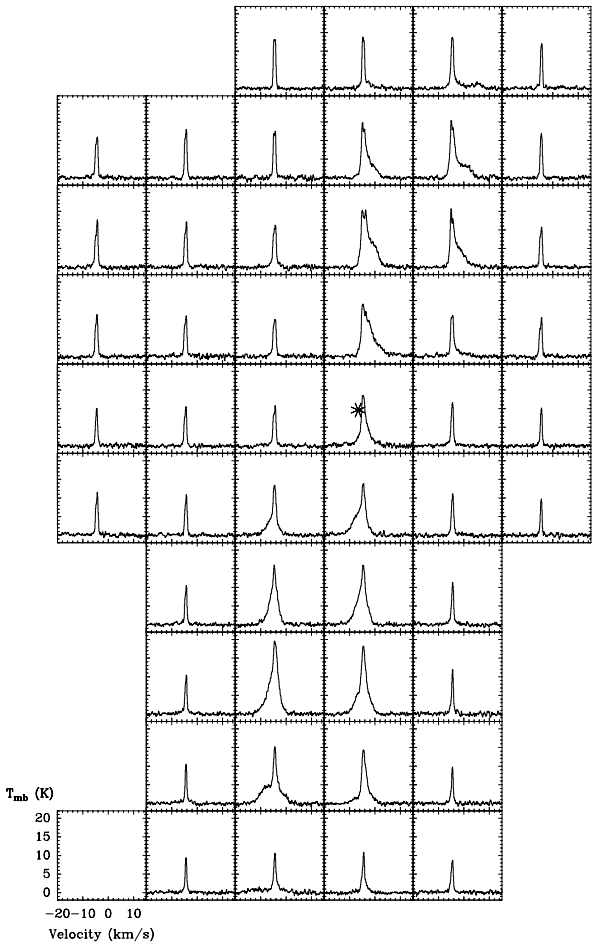

FIG. 4.—^{12}CO $J = 1 \rightarrow 0$ spectra over the $6' \times 10'$ region mapped with position-switching at SEST. The asterisk marks the position of the mm continuum source. The angular separation between panels is 60″. The scale is given in the panel in the lower left.

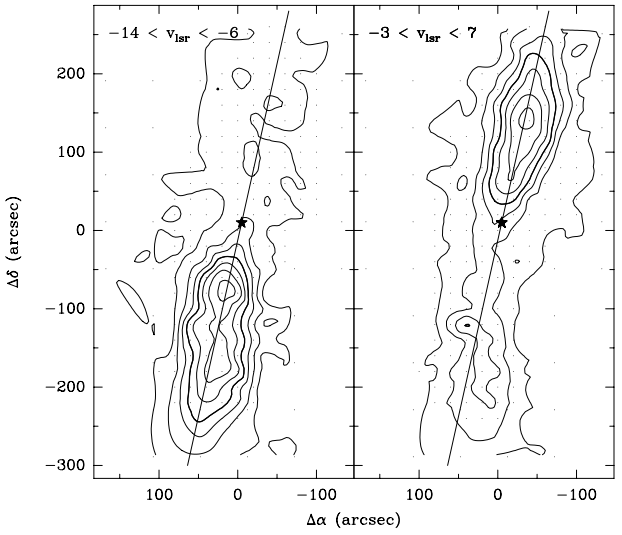

FIG. 5.—*Left*: ^{12}CO $J = 1 \rightarrow 0$ emission integrated over the velocity range $-14 < v_{lsr} < -6$ km s^{-1}, which is blueshifted with respect to the ambient velocity of -4.5 km s^{-1}. *Right*: ^{12}CO $J = 1 \rightarrow 0$ emission integrated over the velocity range $-3 < v_{lsr} < 7$ km s^{-1}, which is redshifted with respect to the ambient velocity. Contours are 5%, 20%, 35%, 50%, 65%, 80%, and 95% of the peak $\int T_{mb}\,dv$ of 36.1 K km s^{-1} in the blue lobe and 44.2 K km s^{-1} in the red lobe. The heavier contour marks the 50% level in each panel. The observed positions are indicated.

strong emission at blueshifted velocities. The emission in the redshifted wing is seen in the LSR velocity range from about -3 to 7 km s^{-1}, and the emission in the blueshifted wing is seen in the range from about -14 to -6 km s^{-1}.

Figure 5 shows the emission in the ^{12}CO $J = 1 \rightarrow 0$ line wings integrated over the velocity range $-14 < v_{lsr} < -6$ km s^{-1} (*left*) and $-3 < v_{lsr} < 7$ km s^{-1} (*right*). Clearly distinguished are two lobes symmetrically placed about the 1.3 mm continuum source (marked with a star—see § 3.3). The bulk of the emission from the southwest lobe arises at velocities that are blueshifted with respect to the ambient cloud velocity, while the bulk of the emission from the northwest lobe arises from velocities that are redshifted. Consequently, we will refer to the southeast lobe as the *blue lobe* and to the northwest lobe as the *red lobe*. The angular size in the direction of the flow of the southeast and northwest lobes are $\sim 5'.3$ and $\sim 5'.0$, respectively, which at a distance of 200 pc translate into linear sizes of 0.31 and 0.29 pc, respectively. From the observed major and minor axes of the lobes we estimate that the semi-opening angle of the outflow is approximately $15° \pm 5°$. The collimation factor is high, with a length-to-width ratio of at least 5 in the lobes, as determined from the half-power contour. The axial alignment of the peaks in the lobes, and the peak in the mm continuum (§ 3.3 and Fig. 13), is very high, suggesting that the ambient medium is relatively homogeneous and/or the outflow source is not precessing significantly. The position angle of the outflow is $\sim 165°$ and is not aligned with either of the globule axes.

3.2.2. *Velocity Structure*

In order to investigate the spatial distribution of the outflowing gas as a function of velocity, we have divided the line wing emission into three pairs of velocity intervals: designated as the high-, intermediate-, and low-velocity intervals, respectively. Each velocity pair is symmetric with respect to the ambient cloud velocity of -4.5 km s^{-1}. The range of velocity integration for the high-velocity pair are from -13.2 to -10.8 km s^{-1} for the blueshifted component and from 1.8 to 4.2 km s^{-1} for the redshifted component; for the intermediate-velocity pair the ranges are from -10.8 to -8.4 km s^{-1} and from -0.6 to 1.8 km s^{-1} for the blueshifted and redshifted components, respectively; finally, for the low-velocity pair the ranges are from -8.4 to -6.0 km s^{-1} and -3.0 to -0.6 km s^{-1} for the blueshifted and redshifted components, respectively. In Figure 6 we present maps of the velocity integrated emission in the six velocity intervals defined above and over the velocity range of the ambient gas emission (middle panel; $-6 < v_{lsr} < -3$ km s^{-1}). It is clear from this figure that in both the high and intermediate-velocity intervals, the blueshifted and redshifted emission arises from two distinct spatially displaced lobes that are symmetric with respect to the flow center. On the other hand, the emission in the low-velocity interval shows superimposed blueshifted and redshifted lobes. These kinematical characteristics can also be appreciated in Figure 7, which shows a position-velocity diagram along the major axis of the outflow. Figure 4 also shows this quite clearly in the high signal-to-noise position-switched observations. In the low-velocity range blueshifted and redshifted emission is observed toward each of the lobes. The observed ^{12}CO emission pattern is in very good agreement with that expected if the flow is viewed nearly perpendicular to its

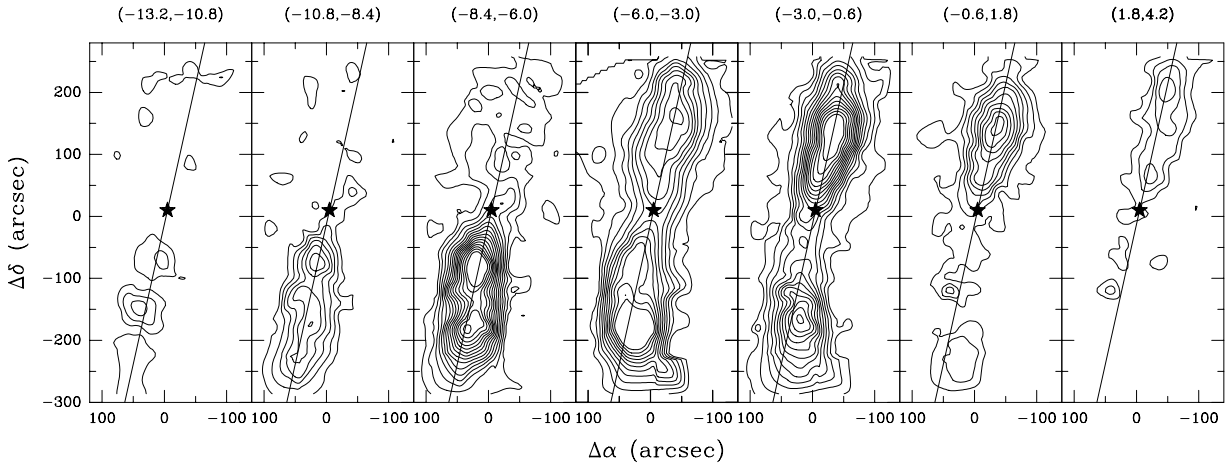

FIG. 6.—^{12}CO $J = 1 \rightarrow 0$ integrated over the high-, intermediate-, and low-velocity channel ranges as described in the text. The velocity range of each panel is indicated. Note that the velocity width is 3.0 km s^{-1} for the central panel, which is the velocity range of the ambient gas (indicated with a heavier border), and 2.4 km s^{-1} for the other panels. Contours are 10–30 K km s^{-1} (interval 2 K km s^{-1}) for the central panel, and 1–15 K km s^{-1} (interval 1 K km s^{-1}) for the other panels. The star marks the position of the mm source and the diagonal line marks the radial axis of the outflow. At the lower velocity intervals (relative to the ambient velocity of −4.5 km s^{-1}), blueshifted and redshifted emission is seen toward both lobes. At higher velocities the outflow becomes more collimated (extreme panels).

symmetry axis, in which case the flow morphology appears as two spatially distinct high-velocity components with superposed blueshifted and redshifted emission (Cabrit & Bertout 1986).

Figure 6 also shows that the spatial extent of the ^{12}CO emission in the three velocity intervals is nearly the same, the lobe sizes showing little dependence on the velocity range. This behavior can neither be explained by a model of an explosive flow that is freely expanding, since in this case the flow should be more extended in the high-velocity range, nor by a decelerated but steady flow, in which case the lobes should be more extended in the low-velocity range (Snell et al. 1984). The independence of lobe size with wing velocity points rather to a model of a steady flow with constant outflow velocity (Cabrit & Bertout 1986; Cabrit, Goldsmith, & Snell 1988). Further, the channel maps in Figure 6 also show that there is a systematic increase in flow collimation with increasing flow velocity.

3.2.3. *Heating of the Ambient Gas by the Outflow*

Figure 6 shows that the integrated emission in the velocity range of the ambient cloud (*middle panel*; $-6 < v_{\rm lsr} < -3$ km s^{-1}) is significantly greater in the outflow lobes than at the position of the embedded mm source. Not only is the integrated intensity greater, but the peak CO intensity in both the $J = 1 \rightarrow 0$ and $J = 2 \rightarrow 1$ transitions is greater toward the outflow lobes (see also Fig. 4). This can be appreciated in Figure 8, which shows spectra at four positions along the outflow axis: one in the red lobe, two in the blue, and at the position of the mm source. This is an unusual result, seen previously in only a few outflows from low-mass sources (e.g., L1157—Umemoto et al. 1992; RNO43—Bence, Richer, & Padman 1996), and it indicates that the excitation temperature of the ambient gas toward the outflow lobes is greater than at the position of the embedded source. The excitation temperature can be estimated from the $J = 2 \rightarrow 1/J = 1 \rightarrow 0$ line intensity ratios (Levreault 1988). To compute these, the $J = 2 \rightarrow 1$ data, taken with a smaller beam, have been convolved with nearby spectra to approximate the beam size of the $J = 1 \rightarrow 0$ data. We find $J = 2 \rightarrow 1/J = 1 \rightarrow 0$ ratios of $\sim$0.85 at the central position and $\sim$0.95 in the lobes. If the lines are optically thick (as suggested by the ^{12}CO $J = 1 \rightarrow 0/^{13}$CO $J = 1 \rightarrow 0$ ratios), then these ratios imply excitation temperatures of less than 15 K at the embedded source position and more than 30 K in the lobes. A similar temperature enhancement was observed by Umemoto et al. (1992) in the outflow from the very red low-mass source IRAS 20386+6751 in L1157. They confirmed the temperature enhancement with observations of ammonia, which indicated kinetic temperatures in excess of 30 K in the outflow lobes (see also Bachiller, Martín-Pintado, & Fuente 1993). If the ambient gas were heated solely by stellar radiation, we would expect the CO maxima to occur at the position of the embedded source (position "mm"). The fact that the peaks occur toward the outflow lobes suggests that the ambient gas there is heated by interactions with the outflow. This heating most likely results from shocks associated with the jet driving the outflow, as discussed later in § 5.1. Our ammonia observations, undertaken before the discovery of the outflow, do not cover the regions of the lobe peaks, so the magnitude of the temperature enhancement in BHR 71 remains to be determined. Observations of the (1, 1) and (2, 2) lines at the offset position $(\Delta\alpha', \Delta\delta') = (0, -1)$ (within the I-band nebulosity) shows only a hint of a slight enhancement in kinetic temperature. However, the signal-to-noise in the (2, 2) spectrum is low, and so any broadening of the (2, 2) line at this position would not be seen in our data.

3.3. *The Embedded Source*

Figure 9 shows a map of the 1.3 mm continuum emission from the central region of BHR 71, revealing a strong compact source with a peak position at $\alpha_{1950} = 11^{\rm h}59^{\rm m}2\overset{\rm s}{.}3$, $\delta_{1950} = -64°52'01''$ (uncertainties in this position are estimated at $1\sigma = 5''$). For comparison, the major and minor axes of the error ellipse of IRAS 11590−6452 are shown (see below). Figure 10 shows a comparison of annular averages centered on the position of peak emission of the mm source with similar averages for Uranus (angular size $3\overset{''}{.}5$) (*upper*), and a decomposition of the profile into two Gaussian components (*lower*). It is clear from Figures 9 and 10

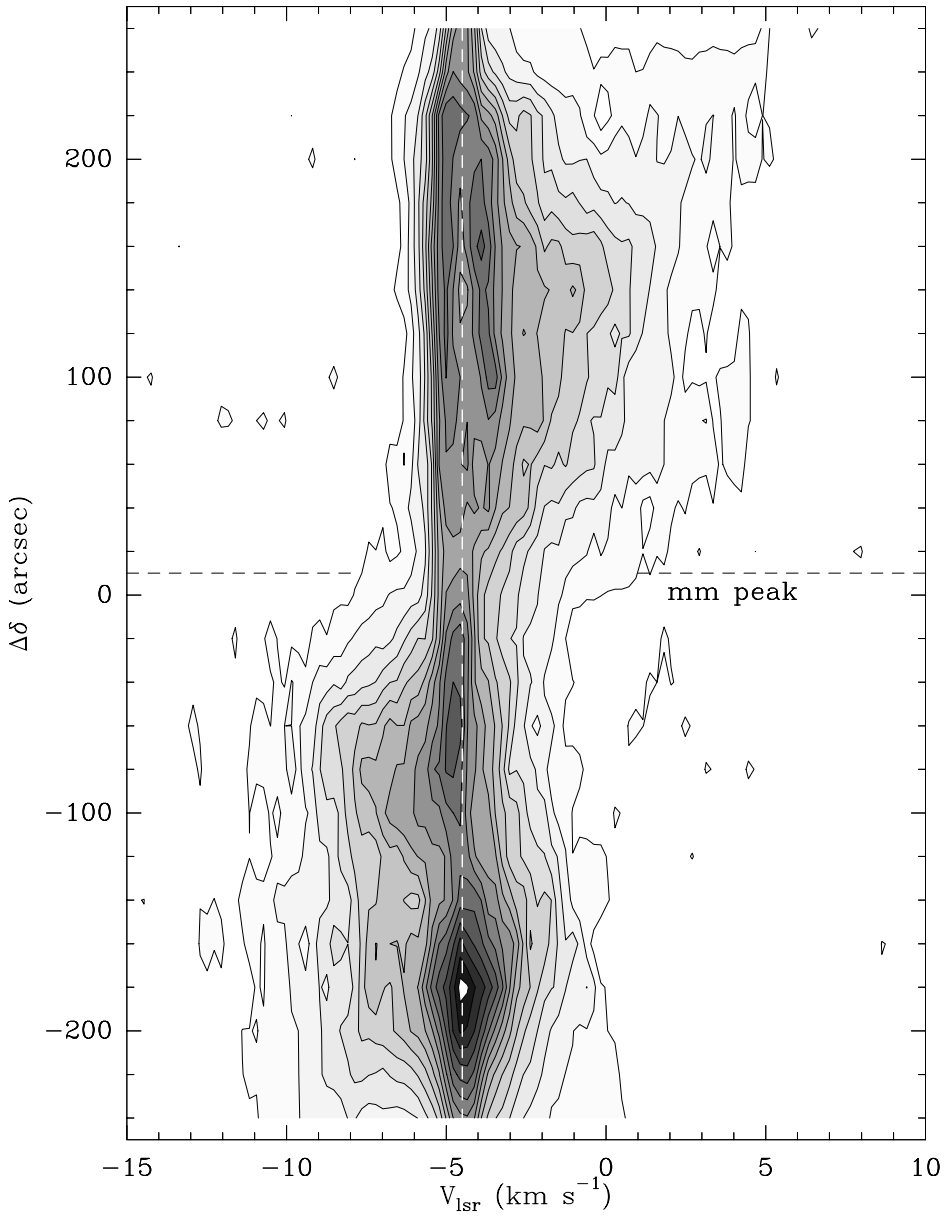

FIG. 7.—Position-velocity diagram of ^{12}CO $J = 1 \rightarrow 0$ along the major axis of the outflow. Contour levels are 1.4–23.8 K by 1.4 K in T_{mb}. The systemic velocity (*vertical dashed line*) and position of the mm peak are as indicated.

that the source as a whole is extended. However, the lower panel of Figure 10 shows that the source profile is well fitted by two Gaussians, a narrow "central" component, and a broad "extended" component, which is also seen in the three best individual maps of the seven made ($\tau < 0.2$) and so is not a result of poor map alignment. Similar two-component continuum structures are observed toward other very young low-mass protostars, e.g., L1448-mm (Guilloteau et al. 1992; Bachiller et al. 1995a) and B335 (Chandler et al. 1990). The central component is unresolved, and the upper limit to its deconvolved FWHM is 7″ (1400 AU). The deconvolved size of the extended component is ~40″ (7600 AU). The peak flux is measured at 2.0 Jy beam^{-1}, and from the continuum map we estimate that the integrated flux in the central component is ~1.7 Jy and in the extended component 2.6 Jy.

Maps of the *IRAS* emission at 12, 25, 60, and 100 μm from a region of equal size to the *I*-band image (Fig. 1) are presented in Figure 11. These maps, made from the co-added images of the Infrared Sky Survey Atlas (ISSA), have been processed with the Maximum Correlation Method (MCM) algorithm (Aumann, Fowler, & Melnyk 1990) at IPAC, and show that there are two infrared sources projected toward the globule: (1) a northern object, IRAS 11589−6447, bright at 12 μm and below the detection limits at the longest wavelength; and (2) a southern object, IRAS 11590−6452, bright at 100 μm and below the detection limits at the shortest wavelength. The peak position of the southern object at 100 μm is $\alpha_{1950} = 11^h59^m03^s.1$, $\delta_{1950} = -64°52'07''$, while that of the northern object at 12 μm is $\alpha_{1950} = 11^h58^m58^s.3$, $\delta_{1950} = -64°48'03''$. In Table 2 we give the flux densities of these objects in the *IRAS* bands taken from the Point Source Catalog (Version 2, 1988, hereafter the PSC). The position of IRAS 11590−6452 is coincident, within the errors, with the position of the 1.3 mm continuum source detected with *SEST* and thus is likely to

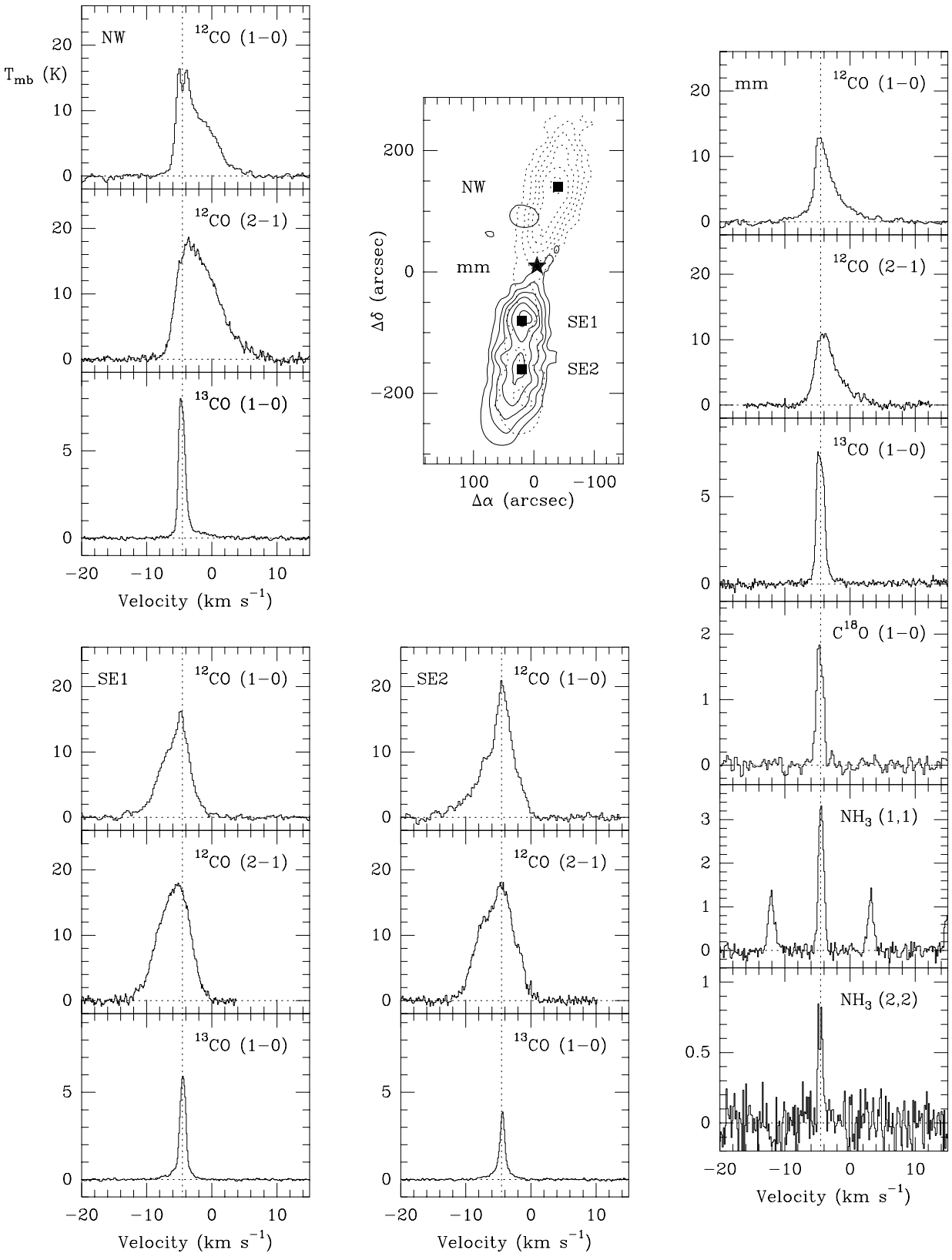

FIG. 8.—Spectra of ^{12}CO $J = 1 \rightarrow 0$ and $J = 2 \rightarrow 1$, ^{13}CO $J = 1 \rightarrow 0$, C^{18}O $J = 1 \rightarrow 0$, and NH_3 $(J, K) = (1, 1)$ and $(2, 2)$, toward select positions in the BHR 71 outflow. Filled squares mark the positions in the outflow map for which we show spectra, with their labels. The star marks the position of the mm continuum peak, for which we also show spectra. The systemic velocity of -4.5 km s^{-1} is indicated for each spectrum.

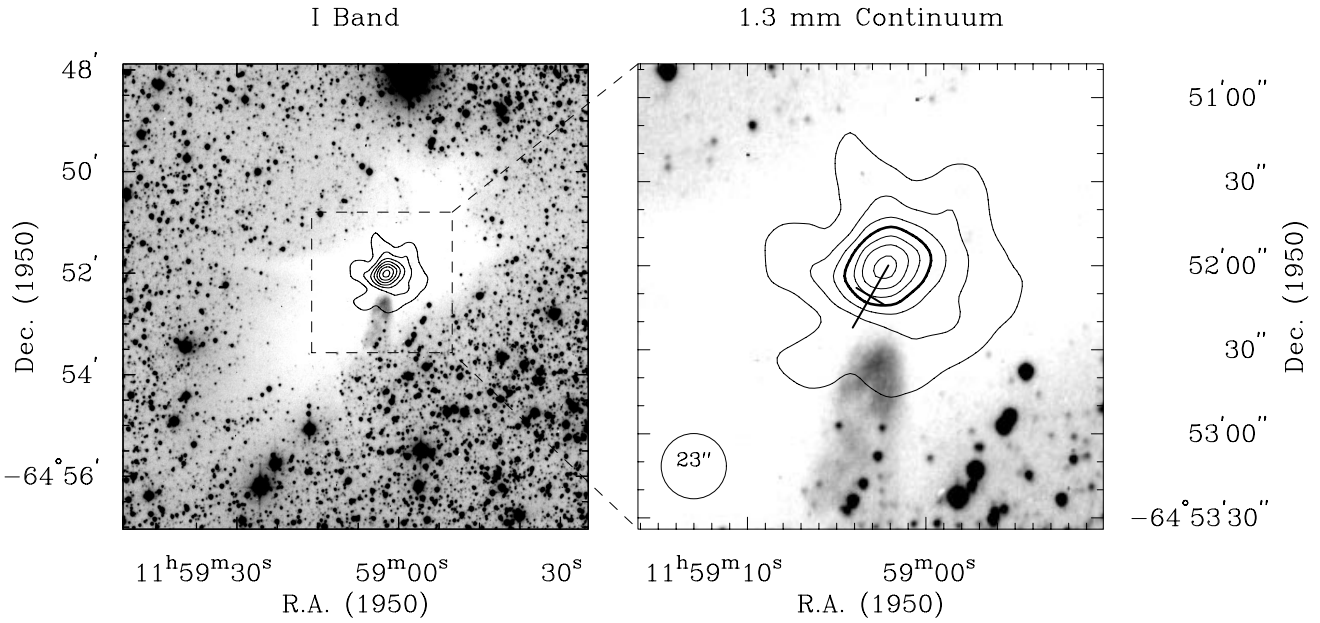

FIG. 9.—1.3 mm continuum emission overlayed on the *I*-band image. *Left*: full field of view for the *I*-band image, showing the relation of the mm emission to the globule. The emission is very well centered on the globule. Contour levels are 5%, 20%, 35%, 50%, 65%, 80%, and 95% of the peak flux of 2 Jy beam^{-1}. *Right*: enlargement of the region indicated on the left panel. The mm continuum is well aligned with the projected apex of the conical reflection nebula. The solid contour is the 50% level, and the cross marks the position and error ellipse of IRAS 11590−6452 as given in the PSC (see text). The beam size is indicated in the lower left of the panel.

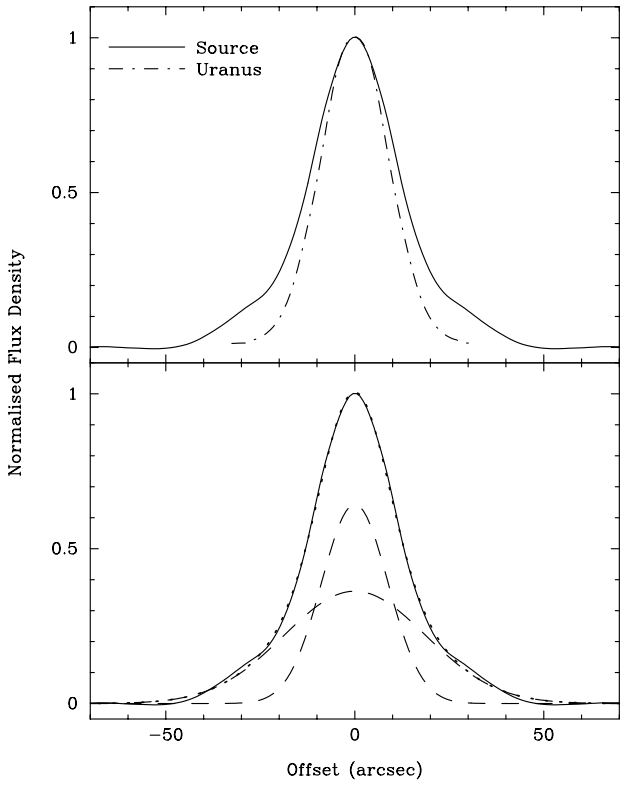

FIG. 10.—*Upper*: normalized profiles of the annularly averaged flux of the mm emission from the continuum source (*solid line*) and Uranus (*broken line*). The offsets for the continuum source are relative to the peak position. *Lower*: the normalized profile of the annularly averaged flux of the mm emission deconvolved into two Gaussian components, as indicated. The composite of the two Gaussians is shown as the dotted line. The FWHM of the beam is 23″.

be associated with the source driving the molecular outflow. IRAS 11589−6447 appears in the *IRAS* catalog of low-resolution spectra (LRS) between 7.7 and 22.6 μm (Olnon et al. 1986). It shows a prominent 10 μm emission band and

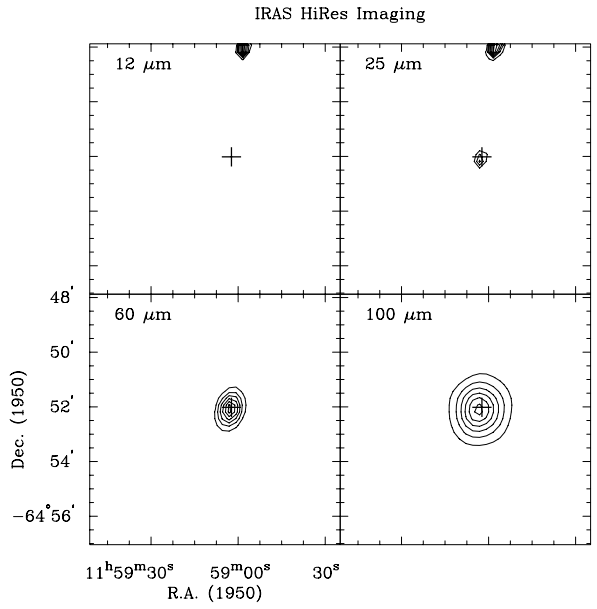

FIG. 11.—Contour maps of the *IRAS* emission toward BHR 71. These co-added maps have been processed by IPAC using the MCM algorithm with 20 iterations. Final beam sizes are estimated at ∼70″ × 38″ for the 12 μm, ∼45″ × 30″ for 25 μm, ∼70″ × 45″ for 60 μm, and ∼105″ × 85″ for 100 μm. Levels are 20%, 35%, 50%, 65%, 80%, and 95% of the peak in each map (1.2 Jy sr^{-1}: 12 μm; 0.53 Jy sr^{-1}: 25 μm; 1.1 Jy sr^{-1}: 60 μm; 0.80 Jy sr^{-1}: 100 μm). The peak position of the mm source is marked with a cross. The image size is the same as that of the *I*-band image (Fig. 1).

TABLE 2

FLUX DENSITIES

Source	$S_{12\,\mu m}$ (Jy)	$S_{25\,\mu m}$ (Jy)	$S_{60\,\mu m}$ (Jy)	$S_{100\,\mu m}$ (Jy)	$S_{1300\,\mu m}$ (Jy)
IRAS 11590−6452.....	0.25L	6.53	77.38	192.90	1.7
IRAS 11589−6447.....	22.02	13.07	2.67	15.41L	...

NOTE.—"L" indicates upper limit only.

has been classified as belonging to the LRS class "29," possibly a star with an O-rich envelope. te Lintel Hekkert et al. (1991) searched for 1612 MHz OH emission toward this source as part of a large survey of candidate OH/IR stars, selected on the basis of their *IRAS* colors. They did not detect any emission. IRAS 11589−6447 can be identified in the *I*-band image as the extremely bright star to the north of the globule.

4. ANALYSIS

4.1. *Physical Properties of the Globule*

4.1.1. ^{12}CO *and* ^{13}CO

The determination of the physical characteristics of the BHR 71 globule is based on the observations of the ^{12}CO $J = 1 \rightarrow 0$ and ^{13}CO $J = 1 \rightarrow 0$ lines at CTIO, and is described in detail in the Appendix. At the peak position we measured a main beam brightness temperature in the ^{12}CO $J = 1 \rightarrow 0$ line of 8.0 K. Assuming that this emission is optically thick and that it completely fills the beam, we find that the excitation temperature of the ^{12}CO $J = 1 \rightarrow 0$ transition is $\sim$11 K. For comparison, Bourke et al. (1995b) derived a rotational temperature between the (1, 1) and (2, 2) inversion transitions of NH_3 of 12 K.

In Table 3 we present observed and derived properties of ^{12}CO and ^{13}CO at nine positions within the globule, separated by about one beamwidth. The optical depth in the ^{12}CO $J = 1 \rightarrow 0$ and ^{13}CO $J = 1 \rightarrow 0$ lines is derived from their ratio of observed brightness temperatures (see eqs. [A2] and [A3]). We find that ^{12}CO is optically thick across the entire mapped region, with $\tau_{12} \sim 40$ near the globule center. For ^{13}CO we determine $\tau_{13} \sim 0.4$ near the center, with only small variations across the mapped region. In columns (9) and (11) of Table 3 we list, respectively, the ^{13}CO opacity and column density at a number of positions within the globule. The column density, as derived from equation (A5) was found to be $N(^{13}\mathrm{CO}) \sim 2.8 \times 10^{15}$ cm^{-2} near the globule center, dropping to $\sim 1 \times 10^{15}$ cm^{-2} at the edges of the map.

The total mass of molecular clouds can be estimated in at least two ways, as given by equation (A6) for the "LTE" mass and equation (A7) for the "CO" mass. For BHR 71 we find $\iint \tau_{13}\, dv\, d\Omega = 106$ km s^{-1} arcmin^2, which assuming an $[H_2/^{13}\mathrm{CO}]$ ratio of 7×10^5 (Frerking, Langer, & Wilson 1982), implies an LTE mass of $\sim 41\ M_\odot$. Alternatively, we find $\iint T_{\rm mb}(^{12}\mathrm{CO})dv\, d\Omega = 2.3 \times 10^3$ K km s^{-1} arcmin^2, implying it has a total molecular (CO) mass of $\sim 39\ M_\odot$.

The average density can be computed from the cloud mass once a cloud geometry is adopted. Assuming that the globule has a spherical morphology, with a diameter equal to the geometric mean of the half-power diameters derived from the deconvolved major and minor axes (as determined from the ^{13}CO observations), and that it is at a distance of 200 pc, implying a cloud radius of 0.25 pc, we find that the globule has an average density of 9×10^3 cm^{-3}.

4.1.2. $C^{18}O$ *and* NH_3

We use the observations of $C^{18}O$ $J = 1 \rightarrow 0$ and NH_3 $(J, K) = (1, 1)$ and (2, 2) to determine the physical characteristics of the dense core. Since the opacity of the ^{13}CO $J = 1 \rightarrow 0$ transition is moderate ($\tau < 0.5$), we can safely assume the $C^{18}O$ $J = 1 \rightarrow 0$ transition is optically thin. The column density of $C^{18}O$ is then given by equation (A8). At the peak of the $C^{18}O$ map we find $N(C^{18}O) = 2.0 \times 10^{15}$ cm^{-2}, which implies $N(H_2) \sim 1.2 \times 10^{22}$ cm^{-2} assuming an $[H_2/C^{18}O]$ ratio of 5.9×10^6 (Rohlfs & Wilson 1996). The total mass traced by $C^{18}O$ may then be found using equation (A9). For BHR 71 we determine $\iint T_{\rm mb}\, dv\, d\Omega = 28.2$ K km s^{-1} arcmin^2, which implies a mass of $\sim 12\ M_\odot$.

Analysis techniques of the NH_3 observations are given in Bourke et al. (1995b). Briefly, the hyperfine components of the (1, 1) inversion transition are modeled to derive the optical depth and excitation temperature at the observed position. The optical depth of the (1, 1) line and the ratio of antenna temperatures of the (2, 2) and (1, 1) transitions may then be used to determine the rotational temperature, and hence the kinetic temperature and volume density. For BHR 71, Bourke et al. (1995b) derive a kinetic temperature at the globule center of 13 K, a mean density for the core of

TABLE 3

^{12}CO AND ^{13}CO OBSERVED AND DERIVED GLOBULE PARAMETERS

OFFSET		OBSERVED						DERIVED		
		^{12}CO			^{13}CO					
Δl (arcmin) (1)	Δb (arcmin) (2)	T_a^* (K) (3)	$V_{\rm lsr}$ (km s^{-1}) (4)	ΔV (km s^{-1}) (5)	T_a^* (K) (6)	$V_{\rm lsr}$ (km s^{-1}) (7)	ΔV (km s^{-1}) (8)	τ_{13} (9)	$\tau_{13}\Delta V$ (km s^{-1}) (10)	$N(^{13}\mathrm{CO})$ (10^{15} cm^{-2}) (11)
−7.50	−7.50	1.95 ± 0.18	−4.39 ± 0.03	0.71 ± 0.07	0.58 ± 0.11	−4.26 ± 0.06	0.72 ± 0.13	0.35	0.26	1.93
0.00	−7.50	4.35 ± 0.24	−4.34 ± 0.02	1.06 ± 0.06	1.24 ± 0.10	−4.30 ± 0.03	0.72 ± 0.06	0.33	0.24	1.82
7.50	−7.50	2.52 ± 0.20	−4.10 ± 0.03	0.86 ± 0.06	0.59 ± 0.11	−4.10 ± 0.05	0.60 ± 0.14	0.27	0.16	1.20
−7.50	0.00	3.79 ± 0.19	−4.42 ± 0.02	0.93 ± 0.04	1.27 ± 0.10	−4.38 ± 0.03	0.77 ± 0.07	0.40	0.31	2.33
0.00	0.00	6.55 ± 0.22	−4.42 ± 0.01	1.09 ± 0.03	2.42 ± 0.09	−4.42 ± 0.01	0.82 ± 0.03	0.46	0.38	2.84
7.50	0.00	2.48 ± 0.20	−4.23 ± 0.03	1.24 ± 0.08	0.59 ± 0.09	−4.34 ± 0.05	0.74 ± 0.10	0.27	0.20	1.49
−7.50	7.50	0.75 ± 0.20	−4.29 ± 0.09	0.82 ± 0.17	0.36 ± 0.11	−4.33 ± 0.07	0.47 ± 0.18	0.66	0.31	2.35
0.00	7.50	2.44 ± 0.18	−4.14 ± 0.03	1.05 ± 0.06	0.41 ± 0.11	−4.30 ± 0.10	0.97 ± 0.19	0.19	0.18	1.35
7.50	7.50	2.69 ± 0.19	−4.01 ± 0.03	1.11 ± 0.06	0.27 ± 0.10	−4.07 ± 0.12	0.82 ± 0.24	0.11	0.09	0.66

NOTE.—Offsets, in galactic coordinates, are relative to $l = 297.^\circ75$, $b = -2.^\circ75$, near the center of the globule.

2.4×10^4 cm^{-3}, and a core mass within the FWHM contour of $\sim 3\ M_\odot$ (corrected for the new distance assumption of 200 pc). From more recent ammonia observations, we find that the kinetic temperature at the offset positions ($\Delta\alpha = \pm 1'$, $\Delta\delta = \pm 1'$) relative to the *IRAS* PSC position shows little variation, with only slight evidence that the temperature drops to 11 K east and west of the center, and increases slightly to the south.

A summary of the observed and derived parameters of the BHR 71 globule are given in Table 4.

4.2. *Molecular Outflow*

4.2.1. *Outflow Inclination*

The dynamics of molecular outflows can, in principle, be elucidated from a comparison of the observed spatial and velocity structure of the flows with synthetic maps. For instance, it should be possible to discern whether the flow is steady or explosive and whether the flow moves with constant velocity or is being accelerated (e.g., Snell et al. 1984). In this spirit, Cabrit & Bertout (1986, 1990) have computed the ^{12}CO line formation in accelerated and constant velocity bipolar outflows, for different values of view angle and flow opening angle. From the observed spatial and kinematical characteristics (e.g., profiles, position-velocity diagrams, etc.), Cabrit & Bertout found that for biconical outflows with power-law velocity fields of the form

$$\boldsymbol{v}(r) = v_0 \left(\frac{r_0}{r}\right)^{\alpha} \hat{\boldsymbol{r}}\ , \qquad (1)$$

where r is the radial distance from the apex of the flow, four cases can be distinguished that depend on the inclination of the outflow axis to the line of sight and the outflow opening angle. These cases are discussed in detail by Cabrit & Bertout.

The observed properties of the outflowing gas from BHR 71 strongly suggest that this molecular outflow is oriented nearly perpendicular to the line of sight and is flowing with a velocity that is nearly independent of the radial distance from the apex. In what follows we assume that the BHR 71 outflow can be modeled by a biconical flow with constant radial velocity (i.e., $\alpha = 0$ in eq. [1]) and derive the values of the model parameters imposed by the observations. First, from the ratio of the observed maximum blueshifted and redshifted velocities within a single lobe, it is possible to estimate the inclination angle, i, of the flow (Cabrit et al. 1988). Using the maximum observed blueshifted and redshifted velocities toward the blue lobe, of ~ 8 and ~ 4 km s^{-1}, respectively, and assuming a semi-opening angle of $15^\circ \pm 5^\circ$, we derive $i = 85^\circ \pm 5^\circ$. Similarly, using the maximum observed redshifted and blueshifted velocities toward the red lobe, of ~ 10 and ~ 3 km s^{-1}, respectively, we find that $i = 82^\circ \pm 5^\circ$. Hereafter, we will adopt an inclination angle for the BHR 71 outflow of 84°. The outflow is thus orientated very close to the plane of the sky. The flow velocity can then be estimated as $V_m/\cos(i - \theta_{\max})$, where V_m is the maximum observed flow velocity. Using the observed value of V_m of ~ 10 km s^{-1} and the derived value for $i - \theta_{\max}$ of $\sim 69^\circ$, we derive a flow velocity of ~ 28 km s^{-1}. Single bipolar outflows with spatial and kinematical characteristics similar to those of the BHR 71 outflow have been observed toward B335 and RNO43 (Cabrit et al. 1988).

4.2.2. *Energetics*

The mass in the lobes can be estimated from the ^{12}CO observations assuming the emission is optically thin, as described in detail in § A2. The main source of error in determing the mass in the outflow arises from the adoption of the velocity boundary between the wing and the ambient line. Further sources of error in this approach are the uncertainties in [H_2/^{12}CO], in the excitation temperature, and the possibility that the ^{12}CO $J = 1 \rightarrow 0$ wing emission might be moderately optically thick at low flow velocities. A general discussion of source of errors in the computation of flow mass have been given by Margulis & Lada (1985) and Cabrit & Bertout (1990).

For the BHR 71 outflow, we will adopt as the velocity boundary of the blue and red wing emission the values of -6 and -3 km s^{-1}, respectively. The lobe emission is integrated over the velocity range $-14 < v_{\rm lsr} < -6$ km s^{-1} in the southeast lobe, and $-3 < v_{\rm lsr} < 7$ km s^{-1} in the northwest lobe (Fig. 5). From the ^{12}CO $J = 1 \rightarrow 0$ and $J = 2 \rightarrow 1$ observations, we determine that $T_{\rm ex} = 11$ K in the southeast lobe and $T_{\rm ex} = 13$ K in the northwest lobe, determined in the manner described in Levreault (1988). Using these temperatures and the observed emission in the velocity ranges given above, we estimated masses of 0.06 and 0.14 $M_\odot$ for the southeast and northwest lobes, respectively. However, as discussed in the previous section, each lobe exhibits emission at both blueshifted and redshifted velocities with respect to the ambient cloud velocity, implying that these masses correspond to a strict lower limit to the total flow mass. In the southeast lobe, the redshifted emission is clearly seen in the integrated velocity map (Fig. 5). The mass arising from redshifted emission in the southeast lobe is estimated to be 0.03 $M_\odot$, so the total mass in the southeast lobe is $\sim 0.09\ M_\odot$. In the northwest lobe, the blueshifted emission is also present, and the mass arising from blueshifted emission in the northwest lobe is $\sim 0.08\ M_\odot$, resulting in a total mass for the northwest lobe of $\sim 0.22\ M_\odot$.

The mass of the low-velocity flow hidden in the ambient cloud range of velocities within the southeast and northwest lobes are estimated, using the method of Margulis & Lada (1985; see also eq. [A16]), to be 0.04 and 0.10 $M_\odot$, respectively. The total mass within each lobe was also estimated

TABLE 4

GLOBULE PARAMETERS

Molecule	$V_{\rm lsr}$ (km s^{-1})	ΔV (km s^{-1})	Diameter[a] (pc)	$\langle N \rangle$[b] (cm^{-2})	$n(H_2)$ (cm^{-3})	Mass ($M_\odot$)
^{12}CO.....	−4.26	1.09	0.66	3.0×10^{17}	4×10^3	39
^{13}CO.....	−4.35	0.80	0.51	2.8×10^{15}	9×10^3	41
C^{18}O.....	−4.63	0.82	0.22	2.0×10^{15}	2×10^4	12
NH_3	−4.45	0.69	0.15	9.2×10^{14}	2×10^4	3

[a] Geometric mean of major and minor axes.

[b] Beam averaged column density.

by simultaneously fitting a broad Gaussian profile (the outflow gas) and a narrow Gaussian profile (the ambient cloud) to the integrated line profiles, obtaining similar masses to the ones quoted above.

From the observations of the ^{12}CO $J = 1 \rightarrow 0$ and ^{13}CO $J = 1 \rightarrow 0$ lines in selected positions of the outflow it is possible to estimate the opacities of the flowing gas and therefore to assess whether or not our assumption that the ^{12}CO $J = 1 \rightarrow 0$ wing emission is optically thin is correct. The average ^{12}CO $J = 1 \rightarrow 0$ opacities in the line wing at different flow positions, computed from equation (A2) using the observed velocity integrated wing emission (third and fourth columns of Table 5) and assuming $T_{ex} = 11$ K (blue lobe) and 13 K (red lobe), and $a = 89$, are listed in the fifth column of Table 5. Typically, the average ^{12}CO $J = 1 \rightarrow 0$ opacities of the blueshifted gas toward the southeast lobe are ~ 2, while the opacities of the redshifted gas toward the northwest lobe are ~ 3, implying that the flowing gas is moderately optically thick. To correct for this effect, we multiply the mass determined from the optically thin assumption by the factor $\tau_w/(1 - e^{-\tau_w})$, where τ_w is the average ^{12}CO $J = 1 \rightarrow 0$ optical depth in the line wing. We find that the opacity-corrected masses within the blue and red lobes ($M_{\rm lobe}$) are ~ 0.23 and ~ 0.69 $M_\odot$, respectively. The opacity corrected masses for the low-velocity material hidden in the ambient line emission ($M_{\rm hidden}$) are 0.09 and 0.30 $M_\odot$, respectively. Adding the lobe masses to the low-velocity masses, we obtained masses of ~ 0.3 and 1.0 $M_\odot$ for the southeast and northwest lobes, respectively.

TABLE 5

OPACITY OF LINE WING EMISSION

Offset Position				
$\Delta\alpha$ (arcmin)	$\Delta\delta$ (arcmin)	$\int T_a(^{12}\mathrm{CO})dv$ (K km s^{-1})	$\int T_a(^{13}\mathrm{CO})dv$ (K km s^{-1})	τ_{12}
Southeast Lobe (Blue)				
−1.0	−5.0	13.1	0.20	0.8
−1.0	−4.0	13.8	0.29	1.6
−1.0	−3.0	8.1	0.46	5.5
−2.0	−4.0	9.2	0.11	0.2
−2.0	−3.0	12.3	0.48	3.7
−2.0	−2.0	15.0	0.47	2.8
Northwest Lobe (Red)				
−2.0	0.0	21.0	0.73	3.2
−2.0	1.0	19.9	0.87	4.2
−2.0	2.0	10.4	0.46	4.3
−3.0	1.0	13.0	0.29	1.8
−3.0	2.0	13.8	0.33	2.0

NOTE.—Offset positions are relative to the OFF position used in the position-switched observations, $\alpha_{1950} = 11^{\rm h}53^{\rm m}44\overset{\rm s}{.}7$, $\delta_{1950} = -65°13'58''$.

From the flow masses it is possible to estimate the momentum P and the kinetic energy E_k in the flow, as well as the mechanical luminosity L_m. A thorough discussion regarding the evaluation of these parameters has been given by Margulis & Lada (1985), Lada (1985) and Cabrit & Bertout (1990), and the relevant equations are given in the Appendix (eqs. [A17] and [A18]). Since for the BHR 71 outflow the radial velocity is approximately constant at 28 km s^{-1} (§ 4.2.1), we will assume $V_{\rm char} = V_0$ for equation (A18), and the parameters determined in this manner are upper limits (Cabrit & Bertout 1990). In Table 6 we give the parameters of the blue and red lobes of the BHR 71 flow calculated using both methods. The dynamical timescale of the outflow, τ_d, is found from R/V_0 and is estimated at $\sim 10^4$ yr. The geometric mean values for the outflow parameters are $P \sim 11\ M_\odot$ km s^{-1}, $E_k \sim 60\ M_\odot$ km^2 s^{-2}, and $L_m \sim 0.5\ L_\odot$.

4.3. *The Energy Source of the Outflow*

The total far-infrared (*IRAS*) luminosity of IRAS 11590−6452 is found to be $L_{IRAS} \sim 8\ L_\odot$ (e.g., Casoli et al. 1986; Parker 1991), assuming a distance of 200 pc. Figure 12 shows the spectral energy distribution (SED) of IRAS 11590−6452 from 12 μm to 1.3 mm, typical of a very young embedded object. According to Lada's (1991) SED classification of low-mass young stellar objects, IRAS 11590−6452 would correspond to an "extreme class I" object, which are characterized by being very weak in the near-infrared ($\lambda \leq 25$ μm) and emitting most of their luminosity at far-infrared and millimeter wavelengths. The emis-

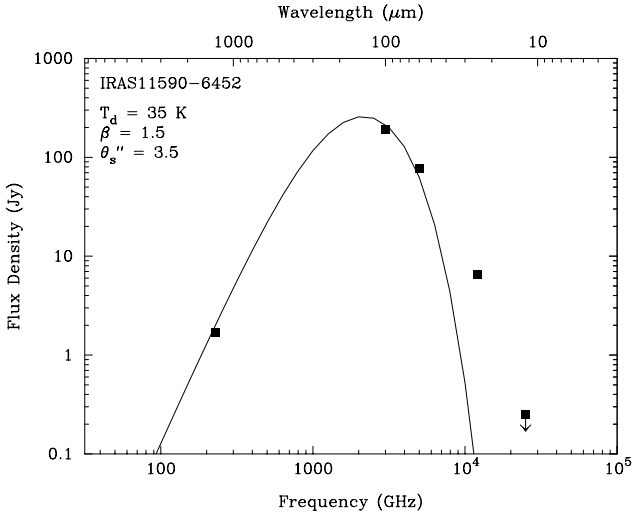

FIG. 12.—Spectral energy distribution of IRAS 11590−6452. The solid curve is a fit to the spectrum with a modified blackbody function of the form $B_\nu(T_d)\{1 - \exp[-(\nu/\nu_0)^\beta]\}$. The parameters used in the fit are indicated on the figure.

TABLE 6

OUTFLOW PARAMETERS

Lobe	$M_{\rm lobe}$ ($M_\odot$)	$M_{\rm hidden}$ ($M_\odot$)	$M_{\rm total}$ ($M_\odot$)	$P^{\rm min}$ ($M_\odot$ km s^{-1})	$P^{\rm max}$ ($M_\odot$ km s^{-1})	$E_k^{\rm min}$ ($M_\odot$ km^2 s^{-2})	$E_k^{\rm max}$ ($M_\odot$ km^2 s^{-2})	$L_m^{\rm min}$ ($L_\odot$)	$L_m^{\rm max}$ ($L_\odot$)	t_d (yr)
SE.....	0.23	0.09	0.32	0.7	9.0	1.5	125	0.004	1.9	10700
NW	0.69	0.32	1.01	2.5	28.3	5.9	396	0.021	6.4	10200
Total.....	0.92	0.41	1.33	3.2	37.3	7.4	521	0.025	8.3	...

NOTE.—$P^{\rm min}$, $E_k^{\rm min}$, $L_m^{\rm min}$ are determined using $M_{\rm lobe}$; $P^{\rm max}$, $E_k^{\rm max}$, $L_m^{\rm max}$ are determined using $M_{\rm total}$.

sion at the longer wavelengths ($\lambda > 25$ μm) can be explained as dust thermal emission arising from a circumstellar shell and is well fitted by a modified blackbody function of the form

$$B_\nu(T_d)[1 - \exp(-\tau_\nu)]\Omega_s , \quad (2)$$

where τ_ν is the dust optical depth, $B_\nu(T_d)$ is the Planck function at the dust temperature T_d, and Ω_s is the solid angle subtended by the dust emitting region. The opacity is assumed to vary with frequency as ν^β, i.e., $\tau_\nu = (\nu/\nu_0)^\beta$, where ν_0 is the frequency at which the optical depth is unity. Due to the limited number of spectral points, we have set the value of β equal to 1.5, consistent with previous values found for very red sources driving highly collimated outflows ($1 < \beta < 2$; AWB; André 1995). We also estimated the dust temperature a priori at 35 K since the good detection at 60 μm suggests that it will be greater than 30 K. The fit is shown in Figure 12. The fact that the 25 μm emission is not fitted by our simple modeling can easily be explained if there exist small grains that are transiently heated to high temperatures, or by emission from within a disk region, or both. The angular size derived for the compact component from the modified blackbody fit to the spectrum is 3".5 (700 AU), assuming a Gaussian flux distribution. However, more detections at the longest wavelengths are required in order to better constrain the fit.

From the fit to the SED we find that the wavelength at which the opacity is unity is $\sim$350 μm, implying that the thermal dust emission at 1.3 mm is optically thin ($\tau_{1.3\ \mathrm{mm}} \sim 0.14$). Thus, the observed flux density at 1.3 mm allows us to estimate the mass of the dense circumstellar material around the driving source of the outflow. Using $T_d = 35$ K and $S_{1.3\ \mathrm{mm}} = 1.7$ Jy in equation (A20) implies a circumstellar mass of 1.0 $M_\odot$ for the unresolved central component. For the extended component, taking $S_{1.3\ \mathrm{mm}} = 2.6$ Jy, we obtain a mass of $M_{\mathrm{cm}} \sim 1.4$ $M_\odot$ (assuming a temperature of 35 K). The total circumstellar mass is therefore $\sim$2.4 $M_\odot$. If the extended component is cooler that 35 K then our mass estimate for this component is a lower limit, e.g., for a temperature of 20 K the mass in the extended component would be 2.8 $M_\odot$. The bolometric luminosity has been estimated in the manner described in Chen et al. (1995), and we find $L_{\mathrm{bol}} \sim 8$ $L_\odot$, the same result as for L_{IRAS}. Integrating under the fitted curve in Figure 12 implies $L_{\mathrm{bol}} \sim 9$ $L_\odot$.

5. DISCUSSION

5.1. *Shocks in A Very Young Outflow*

Figure 13 (Plate 10) presents an overview of the outflow system in BHR 71, with the blue contours representing the blue lobe of the outflow, red contours the red lobe (see Fig. 5), and the black contours representing the 1.3 mm continuum emission (Fig. 9). Figure 13 shows that the outflow is highly collimated, and that the lobes are cylindrical in shape—the outflow angle does not stay constant but becomes narrower as the radial distance from the flow center increases. This implies that we are probably witnessing a very young jet-driven outflow in action (e.g., Masson & Chernin 1993; Raga & Cabrit 1993), where the outflow results from the prompt entrainment of material in the wake of a bow shock created by the jet as it plows through the ambient molecular material. The youth of the outflow is also inferred from the young dynamical age of $\sim 10^4$ yr, and the high degree of collimation of the outflow lobes, particularly the increase in collimation at higher velocities (Bachiller & Gómez-González 1992).

The increase in CO emission, and hence gas kinetic temperature, at the ambient cloud velocity in the direction of the outflow lobes indicates that the outflow is heating the ambient gas in some way. The L1157 outflow, which exhibits similar CO behavior to BHR 71, shows strong evidence for shock excitation in the lines of SiO, CH_3OH, H_2, and NH_3 (3, 3), suggesting that the enhancement seen in BHR 71 is a result of shock heating of the ambient gas by bow shocks at the head of the jet driving the outflow, and supporting the view that the outflow is jet driven (Umemoto et al. 1992; Mikami et al. 1992; Bachiller et al. 1993, 1995b; Davis & Eislöffel 1995; Tafalla & Bachiller 1995; Zhang et al. 1995; Gueth, Guilloteau, & Bachiller 1996). The enhancement of SiO and CH_3OH is thought to be the result of grain destruction caused by the passage of shocks through the ambient medium (Bachiller & Gómez-González 1992), and is believed to be an indicator of outflow evolution, with only the youngest outflows i.e., those that have not yet cleared away the ambient material, showing enhancements in these molecules. We have extensive observations of SiO and CH_3OH toward the outflow in BHR 71 that, like L1157, show strong intensity increases and line wings in the outflow, but little or no emission at the position of the embedded source (Garay et al. 1997, in preparation).

Further evidence for bow shocks come from observations of molecular hydrogen emission in the near-infrared (NIR), which show a close spatial correlation between NIR bow shock structures and limb-brightened cavity structures with the integrated CO lobe emission in the flow (e.g., Bachiller et al. 1995a; Bally, Lada, & Lane 1993; Davis & Eislöffel 1995). In Figure 13 we see that the first peak of CO emission in the blue lobe coincides with the termination of the nebulosity seen in the I-band image. Observations in the NIR (Bourke 1994; Bourke et al. 1997, in preparation) shows extensive molecular hydrogen emission is associated with both the blue and red lobes of the outflow, and that an arclike structure coincides with the first blue peak. Similar structures have been observed in other highly collimated outflows (Davis & Eislöffel 1995), adding further support to the view that shocks are playing a major role in the BHR 71 outflow.

5.2. *Globule Disruption by the Outflow*

One remarkable feature of the outflow is the extent to which it can be traced outside of the optical boundary of the globule, as defined by the I-band extinction. This feature is evident even when comparing the outflow to the image taken in blue light (Fig. 1). A similar phenomena is seen in B335 (Cabrit et al. 1988 and Frerking et al. 1987). The spatial coincidence between the nebulosity and the blue lobe suggests that the outflow may be breaking through the front side of the globule, or at least has carved out a cavity along the outflow axis, with the nebulosity resulting from light scattered into the line of sight by the cavity walls. The stars that may be seen along the line of sight to the nebulosity are most probably background stars, rendered visible due to the decrease in extinction caused by the evacuation of material by the outflow. The fact that the nebulosity is narrow compared to the outflow lobes may add further support to the idea that the outflow is jet driven, and the cavity has resulted from the passage of bow shocks along

the jet that have cleared away the ambient material. The contours of $C^{18}O$ (Fig. 3) provide further evidence that an evacuation is taking place, and that the globule is being disrupted by the outflow. Along the outflow axis toward the blue lobe we see that the $C^{18}O$ contours take a sharp dip toward the globule center, indicating a decrease in column density along the line of sight to the blue lobe. Toward the red lobe the nesting of the $C^{18}O$ contours to higher column density is disrupted, suggesting that the gas in this region has also been disturbed by the outflow.

5.3. *Comparison with the B335 Outflow*

Cabrit et al. (1988) have investigated the properties of the outflow in the well studied Bok globule B335 in a similar manner to this paper. In Table 7 we list the derived properties of the two globules for comparison. Data for B335 are taken from Cabrit et al. (1988; outflow), Frerking et al. (1987; ambient CO), Menten et al. (1984; ambient NH_3), and Benson & Myers (1989; ambient NH_3). In calculating their upper limits, Cabrit et al. did not attempt to correct for the outflow mass hidden in the ambient line core. For Table 7 we have recalculated our upper limits using $M_{\rm lobe}$ as the outflow mass (Table 6), rather than $M_{\rm total}$, which was used in Table 6, to be consistent with Cabrit et al. In this table we introduce quantities used by Cabrit et al., the momentum, or outflow, efficiency ($Fc/L_{\rm bol} \equiv P/t_d \times c/L_{\rm bol}$), and the energy efficiency ($L_m/L_{\rm bol}$). We give only "upper" limit estimates for t_d from Cabrit et al., and we have redetermined $Fc/L_{\rm bol}$ appropriately. We also estimate the mass traced by ammonia for B335 based on the studies of Menten et al. (1984) and Benson & Myers (1989), using the method of Bourke et al. (1995b).

Though the globules have similar masses regardless of the tracer used, the properties of the outflows and central sources are significantly different. The embedded source in B335 has a luminosity of 3 $L_\odot$ and a circumstellar mass of 0.8 $M_\odot$, while the values for the embedded source in BHR 71 are greater by a factor of 3 on both counts. In BHR 71 we are dealing with a more massive and luminous source. The outflow properties are also significantly different. Though both globules have highly collimated outflows, it appears that the outflow in BHR 71 is younger and more energetic, and the central source is more efficient at transferring momentum and energy to its outflow. In fact, all the parameters relating to the dynamics of the outflow, i.e., momentum, kinetic energy, mechanical luminosity, momentum efficiency ($Fc/L_{\rm bol}$), and energy efficiency ($L_m/L_{\rm bol}$), are *at least an order of magnitude greater in the BHR 71 outflow*. However, the spectral characteristics of both outflow sources suggest that the outflows are driven by very young "Class 0" sources (see below).

Thus, while the globules B335 and BHR 71 are similar, the YSO/outflow system in BHR 71 seems to be a scaled up version of the system in B335 in many aspects, i.e., it is more energetic and driven by a more powerful source, but at the same time it is younger.

5.4. *The Nature of the Driving Source*

In § 4.3 we estimated that the total circumstellar mass around IRAS 11590−6452 is $\sim$2.4 $M_\odot$. Whether the bulk of this mass is in the form of a disk, an infalling envelope, or a combination of the two, is not clear. Cabrit & André (1991) found that low-luminosity ($L_{\rm bol} < 100\ L_\odot$) deeply embedded YSO's with well developed molecular outflows have considerably stronger millimeter fluxes than those without flows. The location of the BHR 71 outflow in the normalized 1.3 mm flux density versus bolometric luminosity diagram (see Cabrit & André's Fig. 1) is as expected for a molecular flow with a massive circumstellar disk. Cabrit & André proposed that the dichotomy between outflow and nonoutflow sources is due to the presence of massive circumstellar disk structures around molecular outflow sources, suggesting a connection between circumstellar disk mass and the driving engine of protostellar outflows.

AWB have proposed a new class of protostellar objects, based primarily on their submillimeter observations of a number of young protostars. This new class, the so-called Class 0 sources, are defined as having (1) indirect evidence for the existence of a central YSO (e.g., a molecular outflow), and (2) a SED well characterized by a single modified blackbody with a temperature of $\sim$15–30 K, which implies a high value of $L_{\rm submm}/L_{\rm bol}$, where $L_{\rm submm}$ is the luminosity at wavelengths longer than 350 μm (AWB; André 1995). Property (1) insures that the sources are not pre-protostellar, while property (2) distinguishes them from

TABLE 7

COMPARISON OF PROPERTIES: B335 AND BHR 71

	B335		BHR 71		
PROPERTY	Min	Max	Min	Max	BHR 71/B335
D (pc)	250		200		...
$M(NH_3)$ ($M_\odot$)	2		3		1.5
$M(C^{18}O)$ ($M_\odot$)	11		12		1
M(CO) ($M_\odot$)	36		40		1
$L_{\rm bol}$ ($L_\odot$)	3		9		3
$M_{\rm cm}$ ($M_\odot$)	0.8		2.4		3
$M_{\rm lobe}$ ($M_\odot$)	0.2		0.9		5
P ($M_\odot$ km s^{-1})	0.4	2.2	3.2	25.8	10
E_k ($M_\odot$ km^2 s^{-2})	0.4	10.1	7.4	360	26
L_m ($L_\odot$)	1.7(−4)	1.8(−2)	2.5(−2)	5.7	220
t_d (yr)	9.3(4)		1.0(4)		0.1
$V_{\rm char}$ (km s^{-1})	10		28		3
$Fc/L_{\rm bol}$	70	390	1800	14000	31
$L_m/L_{\rm bol}$	5.6(−5)	5.9(−3)	2.8(−3)	0.6	70

NOTE.—The ratio is the geometric mean of two ratios when a min and max value are quoted. Values in parentheses are powers of 10.

Class I sources, which are more evolved (André 1995). AWB proposed that Class 0 sources be defined as those objects that have $L_{\rm submm}/L_{\rm bol} > 5 \times 10^{-3}$, which in turn implies $M_{\rm cm}/M_* > 1$, where M_* is the mass of the protostellar object (based on assumptions about mass infall rates and circumstellar dust temperatures). This number is meant to indicate that sources with this property "have yet to accrete the bulk of their final stellar mass" (André 1995). For IRAS 11590−6452, we find that $L_{\rm submm}/L_{\rm bol} \sim 2 \times 10^{-2}$. The dust temperature we have used of 35 K is greater than the range defined in property (2), but is similar to values found for other Class 0 candidates, e.g., L1448-mm (Bachiller et al. 1995a).

In a similar vein, André (1995) and Bontemps et al. (1996) have argued that a plot of circumstellar mass against bolometric luminosity (essentially integrated 1.3 mm flux against $L_{\rm bol}$) can be used as an evolutionary indicator. While Reipurth et al. (1993) have shown that there is a correlation between these two properties for Class I sources, the Class 0 sources have circumstellar masses an order of magnitude greater. The location of IRAS 11590−6452 in such a plot not only indicates that it may have a massive circumstellar disk (if Cabrit & André 1991 are correct), but that it is similar to the Class 0 sources in possessing a relatively large circumstellar mass. Bontemps et al. (1996) have also argued that the outflow properties of Class 0 sources are significantly different from the properties of outflows from Class I sources. When they plot outflow momentum flux against $L_{\rm bol}$ they find a good correlation for Class I sources, but outflows from Class 0 sources have a much larger momentum flux. They find that Class I sources have a momentum efficiency ("outflow efficiency") of ∼100 on average, while Class 0 sources have an average value an order of magnitude greater. For the BHR 71 outflow, we estimate an outflow efficiency of ∼5500.

Myers & Ladd (1993) have attempted to classify YSOs on the basis of their "bolometric temperature," $T_{\rm bol}$, which they define as the temperature of a blackbody having the same mean frequency as the observed source SED, the mean frequency being the ratio of the first and zeroth moments of the spectrum. For main-sequence stars, $T_{\rm bol} \equiv T_{\rm eff}$, while for embedded protostellar objects, for which no measure of $T_{\rm eff}$ is possible, and which have spectra much broader that a blackbody, $T_{\rm bol}$ is very low, typically less than 100 K (Chen et al. 1995). Previous determinations of $T_{\rm bol}$ for a large number of sources (Myers & Ladd 1993; Chen et al. 1995) show a clear trend for the youngest sources to have the lowest values of $T_{\rm bol}$ (see Fig. 6 of Chen et al. 1995) and how the use of a log-log diagram of $L_{\rm bol}$ versus $T_{\rm bol}$ (the "BLT" diagram) can distinguish sources of different "classes" in the scheme of Lada (1991). These studies required that in order to calculate $T_{\rm bol}$ the source must have been detected at six or more frequencies. For IRAS 11590−6452, detections at only four frequencies have been made. However, these detections bound the frequency at which the peak emission occurs (Fig. 12), and allows us to estimate that $T_{\rm bol} \sim 56$ K with some confidence. Placing IRAS 11590−6452 on Figure 6 of Chen et al. indicates that it is a Class 0 protostellar source (André 1995).

The high obscuration, cold dust temperature, low bolometric temperature, and significant amount of circumstellar material around IRAS 11590−6452, the central source of BHR 71, are characteristic of Class 0 young stellar objects (e.g., André 1995, and references therein). These objects are thought to be still building up their mass from a surrounding infalling envelope and therefore are at the earliest known stage of evolution of protostars. There are presently about 30 known objects within this class (Bachiller 1996), several of which were discovered because they are associated with highly collimated outflows. We suggest that at the center of BHR 71 lies a very young protostar that is still accreting matter.

6. SUMMARY AND CONCLUSIONS

We have observed the southern Bok globule BHR 71 in the $J = 1 \rightarrow 0$ and $J = 2 \rightarrow 1$ transitions of ^{12}CO, the $J = 1 \rightarrow 0$ transition of ^{13}CO and C^{18}O, in the $(J, K) = (1, 1)$ and (2, 2) inversion transitions of ammonia, and in the continuum at 1.3 mm, with angular resolutions ranging from 20″ to 9′. The main results and conclusions presented in this paper are summarized as follows.

1. The observations of the $J = 1 \rightarrow 0$ ^{12}CO and ^{13}CO lines with low angular resolution (FWHM 8.′8) indicate that the emission arises from roughly a circular region of size ∼0.5 pc. From these observations we derive that the molecular gas has a kinetic temperature of 11 K, an average molecular density of $\sim 9 \times 10^3$ cm^{-3}, and a total mass of $\sim 40\ M_\odot$.

2. C^{18}O emission arises from an elongated structure of size $\sim 0.3 \times 0.15$ pc and mass $12\ M_\odot$, which is spatial correlated with the I-band extinction. The C^{18}O, which traces column density, appears to have been disrupted by the passage of the outflow. The ammonia observations, which sample denser gas, also show an elongated structure, of size $\sim 0.2 \times 0.1$ pc. From these observations we derive that the central region of the globule has a density 2×10^4 cm^{-3} and a kinetic temperature of 13 K. The mass of the dense core traced by ammonia is $3\ M_\odot$.

3. The observations of the $J = 1 \rightarrow 0$ ^{12}CO line emission with high angular resolution (FWHM 45″) reveal the presence, toward the center of the globule, of a highly collimated bipolar outflow with lobes extending by ∼0.3 pc in opposite directions. The bulk of the emission from the southwest lobe arises at velocities that are blueshifted (velocity range from about −14 to −6 km s^{-1}) with respect to the ambient cloud velocity, while the bulk of the emission from the northwest lobe arises from velocities that are redshifted (velocity range from about −3 to 7 km s^{-1}). In addition, both blueshifted and redshifted emission at low outflow velocities ($1.2 < |v - v_0| < 3.6$ km s^{-1}, where v_0 is the ambient cloud velocity) is detected toward each of the lobes. The observed morphology and velocity structure of the flow is well accounted for with a simple model of a biconical outflow with a semi-opening angle of 15°, in which the gas moves outward with a constant radial velocity (with respect to the cone apex) of ∼28 km s^{-1} and that is viewed nearly perpendicular to its symmetry axis. The inclination of the outflow axis from the line of sight is found to be ∼84°.

4. We find that the excitation temperature of the outflowing gas is 11 K in the southeast lobe and 13 K in the northwest lobe. The total flow masses within each lobe, taking into account the mass in the velocity range of the ambient cloud and optical depth effects of the flowing gas, are 0.3 and 1.0 $M_\odot$ for the southeast and northwest lobes, respectively. The mechanical luminosity of the molecular outflow is $\sim 0.5\ L_\odot$, and its dynamical age is $\sim 10^4$ yr.

5. The 1.3 mm continuum observations reveals a strong compact source at the origin of the outflow, which is coincident with the source IRAS 11590−6452, surrounded by an extended component. The total luminosity is $L_{bol} \sim 9$ $L_\odot$. The spectral energy distribution of this object, likely to be associated with the source driving the molecular outflow, is similar to those of circumstellar structures surrounding very young embedded protostellar objects or Class 0 sources in the classification scheme of André et al. (1993). The emission at the longer wavelengths ($\lambda > 25$ μm) can be simply explained as dust thermal emission arising from an extended cold circumstellar structure with a dust temperature of $\sim$35 K (assuming a dust opacity power-law dependence with frequency of $\sim$1.5). We find that the circumstellar mass associated with IRAS 11590−6452 is $\sim$2.4 $M_\odot$.

We conclude that the BHR 71 outflow is a new example of the class of highly collimated molecular outflows that appear to be driven by very young protostellar objects with extremely cold spectral signatures, thought to play a crucial role in the formation of standard bipolar flows. In a forthcoming paper, we will present the results of our observations of CS, SiO, HCO^+, and CH_3OH toward the outflow, which show abundance enhancements similar to those seen toward other highly collimated outflows, in particular the L1157 outflow.

We thank Mario Tafalla for his help with the data reduction and interpretation of the observations presented here, his time spent discussing these unusual highly collimated outflows, and his critical reading of the manuscript. The generous allocation of telescope time by the Onsala/SEST Program Committee and the ATNF TAC is also acknowledged. T. L. B. thanks the School of Physics, ADFA, and the SAO Predoctoral Fellowship program for financial support. G. G. gratefully acknowledges support from a Guggenheim Fellowship and the Chilean FONDECYT project 1950524.

APPENDIX

In this Appendix we summarize the equations that have been used to derive the physical properties of the BHR 71 globule and its molecular outflow.

A1. DERIVATION OF GLOBULE PROPERTIES

A1.1. ^{12}CO *and* ^{13}CO

The main beam brightness temperature of the line emission from a molecular cloud is given by (e.g., Ho, Moran, & Rodríguez 1982)

$$T_{mb} = f[J(T_{ex}) - J(T_{bg})][1 - \exp(-\tau)] , \tag{A1}$$

where τ is the optical depth of the cloud in the molecular transition, f is the filling factor, T_{ex} is the excitation temperature of the transition, T_{bg} is the background temperature, and

$$J(T) = \frac{h\nu}{k} \frac{1}{\exp(h\nu/kT) - 1} .$$

The optical depth in the ^{12}CO $J = 1 \rightarrow 0$ and ^{13}CO $J = 1 \rightarrow 0$ lines can be derived from their ratio of observed brightness temperatures as follows. Using equation (A1) for both lines, we find

$$\frac{1 - \exp(-\tau_{12}/r)}{1 - \exp(-\tau_{12})} = \frac{[J_{12}(T_{ex}) - J_{12}(T_{bg})]}{[J_{13}(T_{ex}) - J_{13}(T_{bg})]} \frac{T_{mb}(^{13}\mathrm{CO})}{T_{mb}(^{12}\mathrm{CO})} , \tag{A2}$$

where r is the τ_{12}/τ_{13} optical depth ratio, given by

$$r = a \frac{1 - \exp(-h\nu_{12}/kT_{ex})}{1 - \exp(-h\nu_{13}/kT_{ex})} \frac{(kT_{ex}/hB_{13} + 1/3)}{(kT_{ex}/hB_{12} + 1/3)} , \tag{A3}$$

where a is the [^{12}CO/^{13}CO] isotopic abundance ratio, and B is the rotational constant of the molecule. Subscripts "12" and "13" refer to the ^{12}CO and ^{13}CO isotopes, respectively. If the excitation temperature is known, these two relations, which are independent of the filling factor, allow the optical depths to be determined. We avoided making the usual approximation that $\tau_{12} \gg 1$, and we solved equation (A2) using an interpolation procedure, assuming a [^{12}CO/^{13}CO] abundance ratio of 89 (Lang 1980).

The total column density N of a linear, rigid rotor, molecule can be derived from the optical depth, τ, and excitation temperature, T_{ex}, of a rotational transition at frequency ν, using the expression (e.g., Garden et al. 1991)

$$N = \frac{3h}{8\pi^3\mu^2} \frac{k(T_{ex} + hB/3k)}{(J+1)hB} \frac{\exp(E_J/kT_{ex})}{1 - \exp(-h\nu/kT_{ex})} \int \tau \, dv , \tag{A4}$$

where μ is the permanent dipole moment and J is the rotational quantum number of the lower state. This expression assumes that all energy levels are populated according to local thermodynamic equilibrium (LTE) at the temperature T_{ex}. In particular the total column density of the ^{13}CO molecule is given, in terms of the opacity and excitation temperature of the $J = 1 \rightarrow 0$

transition, by

$$N(^{13}\mathrm{CO}) = 2.42 \times 10^{14} \frac{T_{\mathrm{ex}} + 0.88}{1 - \exp(-5.29/T_{\mathrm{ex}})} \int \tau_{13}\, dv \,, \tag{A5}$$

where v is measured in km s^{-1}.

The total mass of molecular clouds can be estimated in at least two ways. The first and most straightforward method is through observations of an optically thin molecule, which allows a direct estimate of the mass in the observed molecular species, from which the total mass may be inferred assuming an appropriate abundance ratio. The mass computed in this way is usually called the LTE mass, since typically only one transition is measured and an extrapolation to the total column density is done assuming a local thermodynamic equilibrium (LTE) population. Integrating equation (A5) over the solid angle subtended by the source, we find

$$\left(\frac{M_{\mathrm{LTE}}}{M_\odot}\right) = 0.312 \left(\frac{\mu_m}{2.72 m_{\mathrm{H}}}\right) \left(\frac{[\mathrm{H_2}/^{13}\mathrm{CO}]}{7 \times 10^5}\right) \left(\frac{D}{\mathrm{kpc}}\right)^2 \frac{T_{\mathrm{ex}} + 0.88}{1 - \exp(-5.29/T_{\mathrm{ex}})} \iint \tau_{13}\, dv\, d\Omega \,, \tag{A6}$$

where μ_m is the mean molecular mass per H_2 molecule, m_{H} is the mass of a hydrogen atom, D is the source distance, v is in km s^{-1}, and Ω is in arcmin^2. When ^{13}CO $J = 1 \rightarrow 0$ and ^{12}CO $J = 1 \rightarrow 0$ data are available, the integral on the right-hand side can be directly computed from the opacity of the ^{13}CO line (derived from eqs. [A2] and [A3]) and the observed line width at each position across the molecular cloud.

A second method, commonly used when isotopic lines measurements are not available, is to assume that the H_2 column density, $N(H_2)$, is proportional to the observed velocity integrated ^{12}CO emission, $\int T_{\mathrm{mb}}(^{12}\mathrm{CO})dv$,

$$N(\mathrm{H_2}) = X \int T_{\mathrm{mb}}(^{12}\mathrm{CO})dv \,.$$

Integrating this expression over the solid angle subtended by the cloud, and assuming $X = 2.3 \times 10^{20}$ cm^{-2}/(K km s^{-1}) (e.g., Rohlfs & Wilson 1996; see Combes 1991 for a discussion), we find that the molecular mass, usually referred as the CO mass, is given by

$$\left(\frac{M_{\mathrm{CO}}}{M_\odot}\right) = 0.425 \left(\frac{X}{2.3 \times 10^{20}}\right) \left(\frac{\mu_m}{2.72 m_{\mathrm{H}}}\right) \left(\frac{D}{\mathrm{kpc}}\right)^2 \iint T_{\mathrm{mb}}(^{12}\mathrm{CO})dv\, d\Omega \,, \tag{A7}$$

where v is in km s^{-1} and Ω is in arcmin^2.

A1.2. $C^{18}O$

In the optically thin limit the column density of $C^{18}O$ is given by

$$N(\mathrm{C^{18}O}) = 2.42 \times 10^{14} \frac{T_{\mathrm{ex}} + 0.88}{1 - \exp(-5.27/T_{\mathrm{ex}})} \frac{1}{J(T_{\mathrm{ex}}) - J(T_{\mathrm{bg}})} \int T_{\mathrm{mb}}(\mathrm{C^{18}O})dv \,. \tag{A8}$$

The total mass traced by $C^{18}O$ may then be found using equation (A6) modified for optically thin $C^{18}O$,

$$\left(\frac{M_{\mathrm{LTE}}}{M_\odot}\right) = 2.58 \left(\frac{\mu_m}{2.72 m_{\mathrm{H}}}\right) \left(\frac{[\mathrm{H_2}/\mathrm{C^{18}O}]}{5.9 \times 10^6}\right) \left(\frac{D}{\mathrm{kpc}}\right)^2 \frac{T_{\mathrm{ex}} + 0.88}{1 - \exp(-5.27/T_{\mathrm{ex}})} \frac{1}{J(T_{\mathrm{ex}}) - J(T_{\mathrm{bg}})} \iint T_{\mathrm{mb}}(\mathrm{C^{18}O})dv\, d\Omega \,. \tag{A9}$$

A2. DERIVATION OF MOLECULAR OUTFLOW PROPERTIES

The mass in the lobes of a molecular outflow can be estimated from ^{12}CO observations assuming that the ^{12}CO $J = 1 \rightarrow 0$ flow emission is optically thin. Assuming that the energy levels of ^{12}CO are populated according to local thermodynamic equilibrium, the total ^{12}CO column density at each observed position within each lobe is given by equation (A4). In the optically thin limit

$$N(^{12}\mathrm{CO}) = F(T_{\mathrm{ex}}) \int T_B(v)dv \,, \tag{A10}$$

where

$$F(T_{\mathrm{ex}}) \equiv 2.31 \times 10^{14} \frac{T_{\mathrm{ex}} + 0.92}{1 - \exp(-5.53/T_{\mathrm{ex}})} \frac{1}{J(T_{\mathrm{ex}}) - J(T_{\mathrm{bg}})} \,,$$

and v is measured in km s^{-1}. The mass at each observed position (α, δ) is given by

$$M(\alpha, \delta) = [\mathrm{H_2}/^{12}\mathrm{CO}]\mu_m A(\alpha, \delta) N(^{12}\mathrm{CO}) \,, \tag{A11}$$

where $A(\alpha, \delta)$ is the size of the emitting area at the observed position. For our frequency-switched observations, the emitting area is taken to be a box of dimension equal to the spatial resolution of the observations, i.e., 20″. The mass at each position within the flow traveling at a particular velocity v with respect to the ambient cloud is then given by

$$M(v, \alpha, \delta) = [\mathrm{H_2}/^{12}\mathrm{CO}]\mu_m A(\alpha, \delta) F(T_{\mathrm{ex}}) T_B(v, \alpha, \delta) \Delta v \,, \tag{A12}$$

where Δv is the velocity resolution of the observations. The total mass is then simply (Margulis & Lada 1985)

$$M = \iiint M(v, \alpha, \delta) dv\, d\alpha\, d\delta = [\mathrm{H_2}/^{12}\mathrm{CO}]\mu_m A(\alpha, \delta) F(T_{\mathrm{ex}}) \Delta v \iiint T_B(v, \alpha, \delta) dv\, d\alpha\, d\delta \ . \tag{A13}$$

In practical terms one first performs the spatial integral by summing all the spectra in the region of interest, obtaining

$$M(v) = [\mathrm{H_2}/^{12}\mathrm{CO}]\mu_m A(\alpha, \delta) F(T_{\mathrm{ex}}) \Delta v \sum_{\Omega} T_B(v) \ , \tag{A14}$$

and then summing over the velocity

$$M = \int M(v) dv = \sum_{v} M(v) \ . \tag{A15}$$

To estimate the contribution to the flow mass from the low-velocity material emitting in the same velocity range as the ambient cloud gas we follow the prescription of Margulis & Lada (1985), approximating the integrated brightness emission in this velocity range as

$$\int_{\mathrm{lobe}} \int_{v_b}^{v_r} T_{\mathrm{mb}}\, dv\, d\Omega = \int_{\mathrm{lobe}} \left(\frac{T^b + T^r}{2} \right) (v_r - v_b) d\Omega \ , \tag{A16}$$

where T^b, v_b and T^r, v_r are the brightness temperature and velocity at the blue and red velocity boundaries, respectively.

The momentum P, kinetic energy, E_k, and the mechanical luminosity L_m of the flow may be determined as described by Margulis & Lada (1985), Lada (1985), and Cabrit & Bertout (1990). In the lower limits, these parameters are determined by performing the following integrals in a similar manner to equation (A13):

$$P = \iiint M(v, \alpha, \delta) v\, dv\, d\alpha\, d\delta \ , \qquad E_k = \frac{1}{2} \iiint M(v, \alpha, \delta) v^2\, dv\, d\alpha\, d\delta \ , \qquad L_m = \frac{1}{2R} \iiint M(v, \alpha, \delta) v^3\, dv\, d\alpha\, d\delta \ , \tag{A17}$$

where R is the length of the outflow lobe. These equations assume no correction for flow inclination and so are strict lower limits. Another method is to assume that all the mass is flowing at a velocity characteristic of the entire flow, V_{char}. The flow parameters are then determined by

$$P = M V_{\mathrm{char}} \ , \qquad E_k = \frac{1}{2} M V_{\mathrm{char}}^2 \ , \qquad L_m = \frac{1}{2R} M V_{\mathrm{char}}^3 \ , \tag{A18}$$

where M is the total mass of the lobe. If the maximum observed flow velocity is used as the characteristic velocity, then the values found from equation (A18) are upper limits.

A3. DERIVATION OF CIRCUMSTELLAR MASS

In general, for an isothermal dust source the total mass of circumstellar matter, M_{cm}, is given in terms of the observed flux density, S_ν, at an optically thin frequency, ν, by (e.g., Chini, Krugel, & Wargau 1987)

$$M_{\mathrm{cm}} = \frac{S_\nu D^2}{R_{\mathrm{dg}} \kappa_\nu B_\nu(T_d)} \ , \tag{A19}$$

where κ_ν is the mass absorption coefficient of dust, R_{dg} is the dust-to-gas mass ratio (assuming 10% He), and $B_\nu(T_d)$ is the Planck function at the dust temperature T_d. In particular for observations at 1.3 mm, we can write

$$\left(\frac{M_{\mathrm{cm}}}{M_\odot} \right) = 37 \left(\frac{S_{1.3\ \mathrm{mm}}}{\mathrm{Jy}} \right) \left(\frac{D}{\mathrm{kpc}} \right)^2 \left(\frac{0.007}{R_{\mathrm{dg}}} \right) \left(\frac{1\ \mathrm{cm^2 g^{-1}}}{\kappa_{1.3\ \mathrm{mm}}} \right) \left[\exp\left(\frac{11.04}{T_d} \right) - 1 \right] . \tag{A20}$$

The main source of uncertainty in the conversion of the observed flux density into gas mass is the $R_{\mathrm{dg}} \kappa_\nu$ factor, or total mass opacity, which is a poorly known quantity (e.g., Gordon 1995). For dense and cold protostellar cores, Ossenkopf & Henning (1994) derive a dust opacity at 1.3 mm of $\kappa_{1.3\ \mathrm{mm}} \sim 1\ \mathrm{cm^2\ g^{-1}}$.

REFERENCES

André, P. 1995, Ap&SS, 224, 29
André, P., Ward-Thompson, D., & Barsony, M. 1993, ApJ, 406, 122 (AWB)
Aumann, H. H., Fowler, J. W., & Melnyk, M. 1990, AJ, 99, 1681
Bachiller, R. 1996, ARA&A, 34, 111
Bachiller, R., Cernicharo, J., Martín-Pintado, J., Tafalla, M., & Lazareff, B. 1990, A&A, 231, 174
Bachiller, R., & Gómez-González, J. 1992, Astron. Astrophys. Rev., 3, 257
Bachiller, R., Guilloteau, S., Dutrey, A., Planesas, P., & Martín-Pintado, J. 1995a, A&A, 299, 857
Bachiller, R., Liechti, S., Walmsley, C. M., & Colomer, F. 1995b, A&A, 295, L51
Bachiller, R., Martín-Pintado, J., & Fuente, A. 1993, ApJ, 417, L45
Bachiller, R., Martín-Pintado, J., & Planesas, P. 1991, A&A, 251, 639
Bally, J., Lada, C. J., & Lane, A. P. 1993, ApJ, 418, 322
Barsony, M. 1994, in Clouds, Cores, and Low-mass Stars, ed. D. P. Clemens & R. Barvainis (Provo: ASP), 197
Bence, S. J., Richer, J. S., & Padman, R. 1996, MNRAS, 279, 866
Benson, P. J., & Myers, P. C. 1989, ApJS, 71, 89
Bok, B. J., & Reilly, E. F. 1947, ApJ, 105, 255
Bontemps, S., André, P., Terebey, S., & Cabrit, S. 1996, A&A, 311, 858
Bourke, T. L. 1994, MSc thesis, Univ. New South Wales
Bourke, T. L., Hyland, A. R., & Robinson, G. 1995a, MNRAS, 276, 1052
Bourke, T. L., Hyland, A. R., Robinson, G., & James, S. D. 1993, Proc. Astron. Soc. Australia, 10, 236
Bourke, T. L., Hyland, A. R., Robinson, G., James, S. D., & Wright, C. M. 1995b, MNRAS, 276, 1067
Bronfman, L., Cohen, R. S., Alvarez, H., May, J., & Thaddeus, P. 1988, ApJ, 324, 248

Cabrit, S., & André, P. 1991, ApJ, 379, L25
Cabrit, S., & Bertout, C. 1986, ApJ, 307, 313
———. 1990, ApJ, 348, 530
Cabrit, S., Goldsmith, P. F., & Snell, R. L. 1988, ApJ, 334, 196
Casoli, F., Dupraz, C., Gerin, M., Combes, F., & Boulanger, F. 1986, A&A, 169, 281
Chandler, C. J., Gear, W. K., Sandell, G., Hayashi, S., Duncan, W. D., Griffen, M. J., & Hazell, A. S. 1990, MNRAS, 243, 330
Chen, H., Myers, P. C., Ladd, E. F., & Wood, D. O. S. 1995, ApJ, 445, 377
Chini, R., Krügel, E., & Wargau, W. 1987, A&A, 181, 378
Combes, F. 1991, ARA&A, 29, 195
Davis, C. J., & Eislöffel, J. 1995, A&A, 300, 851
Emerson, D. T., Klein, U., & Haslam, C. G. T. 1979, A&A, 76, 92
Frerking, M. A., Langer, W. D., & Wilson, R. W. 1982, ApJ, 262, 590
———. 1987, ApJ, 313, 320
Fukui, Y., Iwata, T., Mizuno, A., Bally, J., & Lane, A. P. 1993, in Protostars & Planets III, ed. E. H. Levy & J. I. Lunine (Tucson: Univ. Arizona Press), 603
Garden, R. P., Hayashi, M., Gatley, I., Hasegawa, T., & Kaifu, N. 1991, ApJ, 374, 540
Gordon, M. A. 1995, A&A, 301 853
Goss, W. M., Manchester, R. N., Brooks, J. W., Sinclair, M. W., Manefield, G. A., & Danzinger, I. J. 1980, MNRAS, 191, 533
Grabelsky, D. A., Cohen, R. S., Bronfman, L., Thaddeus, P., & May, J. 1987, ApJ, 315, 122
Gueth, F., Guilloteau, S., & Bachiller, R. 1996, A&A, 307, 891
Guide Star Catalog. 1989 (Baltimore: STScI), CD-ROM
Guilloteau, S., Bachiller, R., Fuente, A., & Lucas, R. 1992, A&A, 265, L49
Hartley, M., Manchester, R. N., Smith, R. M., Tritton, S. B., & Goss, W. M. 1986, A&AS, 63, 27
Haslam, C. G. T. 1974, A&AS, 15, 333
Ho, P. T. P., Moran. J. M., & Rodríguez, L. F. 1982, ApJ, 262, 619
IRAS Point Source Catalog, Version 2. 1988, Joint *IRAS* Science Working Group (Washington: GPO) (PSC)
Kreysa, E. 1990, in Proc. 29th Liège Int. Astron. Colloq., From Ground-Based to Space-Borne Sub-mm Astronomy, ed. B. Kaldeich (Noordwijk: ESA), 265
Lada, C. J. 1985, ARA&A, 23, 267
———. 1991, in The Physics of Star Formation and Early Stellar Evolution, ed. C. J. Lada & N. D. Kylafis (Dordrecht: Kluwer), 329
Lang, K. R. 1980, Astrophysical Formulae (Berlin: Springer)
Launhardt, R., & Henning, Th. 1994, in Clouds, Cores, and Low-mass Stars, ed. D. P. Clemens & R. Barvainis (Provo: ASP), 224
Levreault, R. M. 1988, ApJS, 67, 283
Margulis, M., & Lada, C. J. 1985, ApJ, 299, 925
Masson, C. R., & Chernin, L. M. 1993, ApJ, 414, 230
Menten, K. M., Walmsley, C. M., Krügel, E., & Ungerechts, H. 1984, A&A, 137, 108
Mikami, H., Umemoto, T., Yamamoto, S., & Saito, S. 1992, ApJ, 392, L87
Myers, P. C. 1995, in Molecular Clouds and Star Formation, ed. C. Yuan & J. You (Singapore: World Scientific), 47
Myers, P. C., & Ladd, E. F. 1993, ApJ, 413, L47
Mundt, R. 1988, in Formation and Evolution of Low-mass Stars, ed. A. K. Dupree & M. T. V. T. Lago (Dordrecht: Kluwer), 257
Olnon, F. M., Raimond, E., Neugebauer, G., van Duinen, R. J., & Habing, H. J. 1986, A&AS, 65, 607
Ossenkopf, V., & Henning, Th. 1994, A&A, 291, 943
Parker, N. D. 1991, MNRAS, 251, 63
Raga, A. C., & Cabrit, S. 1993, A&A, 278, 267
Reipurth, B. 1991, in The Physics of Star Formation and Early Stellar Evolution, ed. C. J. Lada & N. D. Kylafis (Dordrecht: Kluwer), 497
Reipurth, B., Chini, R., Krügel, E., Kreysa, E., & Sievers, A. 1993, A&A, 273, 221
Rodgers, A. W. 1960, MNRAS, 120, 163
Rohlfs, K., & Wilson T. L. 1996, Tools of Radio Astronomy (2d. ed.; Berlin: Springer)
Sandqvist, A. 1977, A&A, 57, 467
Seidensticker, K. J., & Schmidt-Kaler, Th. 1989, A&A, 225, 192
Snell, R. L., Scoville, N. Z., Sanders, D. B., & Erickson, N. R. 1984, ApJ, 284, 176
Tafalla, M., & Bachiller, R. 1995, ApJ, 443, L37
te Lintel Hekkert, P., Caswell, J. L., Habing, H. J., Haynes, R. F., & Norris, R. P. 1991, A&AS, 90, 327
Umemoto, T., Iwata, T., Fukui, Y., Mikami, H., Yamamoto, S., Kameya, O., & Hirano, N. 1992, ApJ, 392, L83
Yun, J. L., & Clemens, D. P. 1990, ApJ, 365, L73
———. 1994, AJ, 108, 612
———. 1995, AJ, 109, 742
Zhang, Q., Ho, P. T. P., Wright, M. C. H., & Wilner, D. J. 1995, ApJ, 451, L71